CVEM-BEM Coupling for the Simulation of Time-Domain Wave Fields Scattered by Obstacles with Complex Geometries

Research Article

Luca Desiderio*, Silvia Falletta, Matteo Ferrari and Letizia Scuderi

CVEM-BEM Coupling for the Simulation of Time-Domain Wave Fields Scattered by Obstacles with Complex Geometries

https://doi.org/10.1515/cmam-2022-0084
Received April 6, 2022; revised December 7, 2022; accepted January 18, 2023

Abstract: In this paper, we present a numerical method based on the coupling between a Curved Virtual Element Method (CVEM) and a Boundary Element Method (BEM) for the simulation of wave fields scattered by obstacles immersed in homogeneous infinite media. In particular, we consider the 2D time-domain damped wave equation, endowed with a Dirichlet condition on the boundary (sound-soft scattering). To reduce the infinite domain to a finite computational one, we introduce an artificial boundary on which we impose a Boundary Integral Non-Reflecting Boundary Condition (BI-NRBC). We apply a CVEM combined with the Crank–Nicolson time integrator in the interior domain, and we discretize the BI-NRBC by a convolution quadrature formula in time and a collocation method in space. We present some numerical results to test the performance of the proposed approach and to highlight its effectiveness, especially when obstacles with complex geometries are considered.

Keywords: Unbounded Domain, Wave Propagation Problems, Complex Geometries, Curved Virtual Element Method, Convolution Quadrature, Boundary Element Method, Non-Reflecting Boundary Condition

MSC 2010: 65N38, 65N99, 65N12, 65N15

1 Introduction

Time-domain wave scattering problems in infinite or very large media appear in many fields of engineering and applied physics such as, for example, acoustics, geophysics and seismology. The development and the analysis of numerical methods for the approximation of the solution of Partial Differential Equations (PDEs) that model these phenomena is a very challenging task, due to the intrinsic difficulty of treating unbounded domains. For this reason, in recent years, the interest of the scientific and industrial communities in the topic has increased, and many efficient methodologies have been proposed. A well-established procedure consists in reformulating the original PDE as a Boundary Integral Equation (BIE), whose discretization is referred to as Boundary Element Method (BEM). In the history of time-domain BIE methods, a milestone is the weak formulation proposed by Bamberger and Ha Duong in [7], forerunner of a lot of contributions that enriched the range of applications of the BEM. Among the main benefits of BEMs, we mention the possibility to reduce the spatial problem dimension by one, and to represent the wave field in the unbounded region only by a discretization of the obstacle boundary. However, a well-known drawback is that the linear BEM systems are populated by blocks of dense matrices so that acceleration techniques are usually employed. Most of them are based on the compression of the underlying matrices in order to apply efficient direct or iterative solvers (see e.g. fast multiple methods [41],

***Corresponding author: Luca Desiderio,** Department of Mathematical, Physical and Computer Sciences, University of Parma, Parma, Italy, e-mail: luca.desiderio@unipr.it. https://orcid.org/0000-0002-3924-0939
Silvia Falletta, Matteo Ferrari, Letizia Scuderi, Department of Mathematical Sciences “G. L. Lagrange”, Polytechnic of Turin, Turin, Italy, e-mail: silvia.falletta@polito.it, matteo.ferrari@polito.it, letizia.scuderi@polito.it. https://orcid.org/0000-0002-4957-3972, https://orcid.org/0000-0002-2577-1421, https://orcid.org/0000-0002-1685-9608

panel clustering [30], hierarchical matrices [18], adaptive cross approximation [2] and wavelet techniques [21]). However, irrespective of the BEM approaches and of their particular implementation, the reconstruction of the field of the original PDE at points of the exterior domain entails a post-processing evaluation of boundary integrals which involve the computed boundary density. This procedure may be not efficient, especially when the solution has to be evaluated in an entire region surrounding the physical obstacle and the boundary has a complex geometry. This is also the case because in its vicinity the boundary integrals have near singularities, whose non-trivial evaluation must be suitably performed.

Alternatively to the pure BEM, when the scattering phenomenon is of interest in a particular area surrounding the obstacle and/or when the medium presents inhomogeneities within a bounded region, it is convenient to introduce an artificial boundary and to reduce the original domain to a finite computational one, neglecting the infinite residual sector. Then the new problem, defined in a bounded region, can be solved by domain methods such as, for example, the classical Finite Element Method (FEM) or finite differences. In order to prevent spurious reflections, which could eventually pollute the solution, a suitable transparent Non-Reflecting Boundary Condition (NRBC) has to be imposed on the artificial boundary. Even if in the last decades a great effort has been devoted to design high-order local NRBCs (see [35]), in the applications, those of Boundary Integral (BI) type are more popular. These latter, besides being exact and suited for outgoing and incoming waves, can be defined on artificial boundaries of general shapes. The global scheme, obtained by combining finite element with boundary element methods, is usually referred to as FEM-BEM coupling.

Many approaches of this type have been proposed in literature, among which we mention the Costabel–Han [3, 10, 20, 33, 34, 36] and the Johnson–Nédélec [26, 37] couplings. The former involves a couple of BIEs and results quite onerous from the computational point of view, due to the presence of a hypersingular boundary integral operator; on the contrary, the latter (also known as the *one-equation* coupling) is based on a single BIE and involves only weakly singular and singular operators. Furthermore, contrary to the Costabel–Han approach, the Johnson–Nédélec one exhibits some technical difficulties in the theoretical analysis. For this reason, nowadays, this latter has been developed only for time independent problems (see [40, 44]). Nevertheless, due to the easiness of its implementation, the one-equation coupling is widely used to address many engineering problems (see, for example, [4] and the references therein).

Very recently, the authors have proposed an approach based on the coupling between the one-equation BEM (collocation or Galerkin) and the (standard or curved) Virtual Element Method (VEM) for the numerical solution of exterior Helmholtz problems [23, 24]. This strategy revealed to be efficient and accurate, even for obstacles with complex geometries. Later, the same procedure has been applied to Poisson problems [22] with decoupled approximation orders, which allowed to retrieve high accuracy by a high-order VEM and a low-order BEM. This aspect is crucial since, for the success of the strategy, tailored quadrature techniques would be needed for the accurate computation of high-order BEM matrices.

The effectiveness of the proposed approach mainly relies on the properties of the VEM which, originally introduced in [11, 12], is a domain method dealing with polygonal or polyhedral mesh elements, on which local discrete spaces and sets of degrees of freedom are defined in such a way that suitable polynomial projections are exactly computable. Consequently, the elementary mass and stiffness matrices are computed without the need of explicitly knowing the expression of the basis functions, with easiness of implementation even for high approximation orders. Such advantages have encouraged the application of VEMs to a wide variety of problems (see [5, 6, 16] for recent results). To the best of the authors' knowledge, VEM-BEM couplings for exterior wave propagation problems have been considered only in the frequency-domain (see the above mentioned [23, 24] and [31]).

In this paper, we fill this gap by considering 2D sound-soft time-domain wave propagation problems in homogeneous media, with scatterers of generic shape, including curvilinear edges. For their numerical solution, on the basis of the results obtained in [21, 23, 24], we propose the coupling between a Curved VEM (CVEM) and a BEM, with decoupled space approximation orders. In particular, in the interior of the computational domain, we propose a Galerkin discretization by means of a CVEM, combined with the Crank–Nicolson scheme in time. We choose a CVEM instead of a standard (polygonal) VEM since the use of curvilinear elements allows us to avoid the approximation of the geometry and to retrieve the optimal rate of convergence for accuracy orders higher than 2, even when dealing with curvilinear obstacles. For the discretization of the BI-NRBC, we apply the Lubich Convolution Quadrature (CQ) method [38], based on A-stable second-order ODE solvers for the approx-

imation in time of the integrals therein involved, coupled with a classical collocation BEM in space. The CQ formulas have the fundamental property of using the Laplace transform of the integral kernels involved in the BI-NRBC instead of their space-time expression, the former having better smoothness properties. Moreover, the quadrature weights can be computed simultaneously by applying the Fast Fourier Transform (FFT) algorithm, and hence the computational complexity of the time discretization is reduced to the order $N \log N$ (N being the number of time instants). For these properties, the CQ formulas have become a very appealing tool for the numerical simulation of wave propagation problems and have been applied in several contexts.

The paper is organized as follows. In the next section, we present the model problem for the time-domain sound-soft scattering, its restriction to a bounded region of interest by the introduction of the BI-NRBC and the variational formulation associated to the problem reformulated in the finite computational domain. In Section 3, we detail the time discretization of the problem, while in Section 4, we describe the main steps that lead to its space discretization. Section 5 is devoted to the algebraic reformulation of the fully discrete scheme. Numerical results, validating the performance of the proposed approach, are illustrated and discussed in Section 6. Finally, some conclusions are drawn and perspectives are given.

2 The Model Problem

In a fixed Cartesian coordinate system $\mathbf{x} = (x_1, x_2)$, we consider an open bounded domain $\Omega_0 \subset \mathbf{R}^2$ with Lipschitz boundary Γ_0 having positive Hausdorff measure. We denote by $\Omega_e := \mathbf{R}^2 \setminus \overline{\Omega}_0$ the exterior unbounded domain in which we consider the damped scalar wave equation

$$\ddot{u}_e(\mathbf{x}; t) + a\dot{u}_e(\mathbf{x}; t) - c^2 \Delta u_e(\mathbf{x}; t) = 0, \quad \mathbf{x} \in \Omega_e,\ t \in [0, T]. \tag{2.1}$$

Here and elsewhere, the superposed dot stands for time differentiation, Δ denotes the Laplace operator, u_e is the unknown wave field, T is the final time of interest, $c > 0$ and $a \geq 0$ are the constant wave speed and damping parameter, respectively. Equation (2.1) is endowed with null initial conditions

$$u_e(\mathbf{x}; 0) = \dot{u}_e(\mathbf{x}; 0) = 0, \quad \mathbf{x} \in \Omega_e,$$

and a Dirichlet boundary condition

$$u_e(\mathbf{x}; t) = g(\mathbf{x}; t), \quad \mathbf{x} \in \Gamma_0,\ t \in [0, T],$$

with $g(\cdot\,; t) \in H^{\frac{1}{2}}(\Gamma_0)$ for all $t \in [0, T]$. In the context of scattering problems, the Dirichlet datum g coincides with the opposite of an incident wave u_{inc} along the boundary of the obstacle, i.e. $g(\mathbf{x}; t) = -u_{\text{inc}}(\mathbf{x}; t)$ on $\Gamma_0 \times [0, T]$.

To retrieve the solution in a bounded region, as many practical applications require, we truncate Ω_e by introducing an artificial boundary Γ, which divides the original domain into two subdomains: an infinite exterior one Ω_∞ and a finite computational one Ω, bounded internally and externally by Γ_0 and Γ, respectively.

In what follows, u and u_∞ stand for the restrictions of the solution u_e to Ω and Ω_∞, and $\mathbf{n}$ and $\mathbf{n}_\infty$ for the unit normal vectors to Γ pointing outside Ω and Ω_∞, respectively. Denoting by $*$ the convolution product, defined as

$$u(t) * v(t) := \int_0^t u(t - \tau) v(\tau)\, \mathrm{d}\tau,$$

we consider the following BIE associated to the solution u_∞ on $\Gamma \times [0, T]$:

$$\frac{1}{2} u_\infty(\mathbf{x}; t) = \int_\Gamma G(\mathbf{x}, \mathbf{y}; t) * \frac{\partial u_\infty}{\partial \mathbf{n}_\mathbf{y}}(\mathbf{y}; t)\, \mathrm{d}\Gamma_\mathbf{y} - \int_\Gamma \frac{\partial G}{\partial \mathbf{n}_\mathbf{y}}(\mathbf{x}, \mathbf{y}; t) * u_\infty(\mathbf{y}, t)\, \mathrm{d}\Gamma_\mathbf{y},$$

which expresses the natural relation between u and its normal derivative at each point of the artificial boundary, and which will be then used as exact (non-local) BI-NRBC. The kernel G is the fundamental solution of the 2D damped wave equation, whose expression is given by

$$G(\mathbf{x}, \mathbf{y}; t) := \frac{c}{2\pi} \cosh\Big(\frac{a}{2c} \sqrt{c^2 t^2 - r^2} \Big) \frac{H[ct - r]}{\sqrt{c^2 t^2 - r^2}} e^{-\frac{a}{2} t}, \tag{2.2}$$

where $r := \|\mathbf{x} - \mathbf{y}\|$ represents the distance between the source point $\mathbf{x}$ and the field point $\mathbf{y}$, and $H[\,\cdot\,]$ denotes the Heaviside function. Note that, when $\alpha = 0$, G is the fundamental solution of the classical 2D wave equation. Taking into account the compatibility and equilibrium conditions

$$u(\mathbf{x};t) = u_\infty(\mathbf{x};t), \quad \frac{\partial u}{\partial \mathbf{n}}(\mathbf{x};t) = -\frac{\partial u_\infty}{\partial \mathbf{n}_\infty}(\mathbf{x};t) \quad (\mathbf{x};t) \in \Gamma \times [0,T],$$

the new problem defined in the domain of interest Ω takes the form

$$\begin{cases} \ddot{u}(\mathbf{x};t) + \alpha \dot{u}(\mathbf{x};t) - c^2 \Delta u(\mathbf{x};t) = 0, & (\mathbf{x};t) \in \Omega \times [0,T], \quad (2.3a) \\ u(\mathbf{x};t) = g(\mathbf{x};t), & \mathbf{x} \in \Gamma \times [0,T], \quad (2.3b) \\ u(\mathbf{x};0) = \dot{u}(\mathbf{x};0) = 0, & \mathbf{x} \in \Omega, \quad (2.3c) \\ \frac{1}{2} u(\mathbf{x};t) + V \frac{\partial u}{\partial \mathbf{n}}(\mathbf{x};t) - K u(\mathbf{x};t) = 0, & \mathbf{x} \in \Gamma \times [0,T], \quad (2.3d) \end{cases}$$

where V and K denote the well-known single- and double-layer integral operators defined by

$$V\psi(\mathbf{x};t) := \int_\Gamma G(\mathbf{x},\mathbf{y};t) * \psi(\mathbf{y};t)\, d\Gamma_\mathbf{y}, \qquad (\mathbf{x},t) \in \Gamma \times [0,T], \quad (2.4)$$

$$K\varphi(\mathbf{x};t) := \int_\Gamma \frac{\partial G}{\partial \mathbf{n}_\mathbf{y}}(\mathbf{x},\mathbf{y};t) * \varphi(\mathbf{y};t)\, d\Gamma_\mathbf{y}, \quad (\mathbf{x},t) \in \Gamma \times [0,T]. \quad (2.5)$$

To obtain a well-posed coupling between the interior PDE and the BIE, we introduce the unknown λ defined on the boundary Γ, that a posteriori will be $\frac{\partial u}{\partial \mathbf{n}}$, and we consider the weak form of (2.3a) and the strong one for (2.3d). To this end, for $f \in H^{\frac{1}{2}}(\Gamma)$, we introduce the space

$$H^1_{f,\Gamma_0}(\Omega) := \{u \in H^1(\Omega) : u|_{\Gamma_0} = f\},$$

the bilinear forms $a\colon H^1(\Omega) \times H^1(\Omega) \to \mathbf{R}$ and $m\colon L^2(\Omega) \times L^2(\Omega) \to \mathbf{R}$,

$$a(u,v) := \int_\Omega \nabla u(\mathbf{x}) \cdot \nabla v(\mathbf{x})\, d\mathbf{x}, \quad m(u,v) := \int_\Omega u(\mathbf{x}) v(\mathbf{x})\, d\mathbf{x}, \quad (2.6)$$

and the duality pairing $\langle\,\cdot\,,\cdot\,\rangle$ on $H^{-\frac{1}{2}}(\Gamma) \times H^{\frac{1}{2}}(\Gamma)$.

Setting $u(t) := u(\mathbf{x};t)$, $\lambda(t) := \lambda(\mathbf{x};t)$ and $g(t) := g(\mathbf{x};t)$, the variational formulation of problem (2.3) consists in the following: for each $t \in [0,T]$, find $u(t) \in H^1_{g(t),\Gamma_0}(\Omega)$ and $\lambda(t) \in H^{-\frac{1}{2}}(\Gamma)$ such that, for all $w \in H^1_{0,\Gamma_0}(\Omega)$, we have

$$\begin{cases} m(\ddot{u}(t),w) + \alpha m(\dot{u}(t),w) + c^2 a(u(t),w) - \langle \lambda(t), w\rangle = 0, & (2.7a) \\ u(0) = \dot{u}(0) = \lambda(0) = 0, & (2.7b) \\ \frac{1}{2} u(\mathbf{x};t) + V\lambda(\mathbf{x};t) - Ku(\mathbf{x};t) = 0, \quad \mathbf{x} \in \Gamma. & (2.7c) \end{cases}$$

3 Discretization in Time

We consider a decomposition of the time interval $[0,T]$ consisting of $N+1$ equally spaced instants $t_n := n\Delta_t$, $n = 0,\dots,N$, $\Delta_t := T/N$ denoting the time step size. First, we describe the time-marching scheme associated to the interior domain method, and then that associated to the BI-NRBC on Γ. These are defined by the Crank–Nicolson scheme and a CQ, respectively, which are both of second (convergence) order. Although in principle other methods can be considered, we have chosen the Crank–Nicolson scheme, which revealed to be efficient and unconditionally stable (even for large time intervals of analysis), here and in other contexts (see [26, 27, 29]).

Discretization of the Variational Problem by the Crank–Nicolson Scheme

We start by introducing the new unknown $v(t) := \dot{u}(t)$ associated to the second-order ODE system (2.7a)-(2.7b) and we reformulate the variational problem as follows:

$$\begin{cases} m(\dot{v}(t), w) + \alpha m(v(t), w) + c^2 a(u(t), w) - \langle \lambda(t), w \rangle = 0, \\ \dot{u}(t) = v(t), \\ u(0) = v(0) = \lambda(0) = 0. \end{cases}$$

Denoting by u^n, v^n and λ^n the approximations of $u(t_n)$, $v(t_n)$ and $\lambda(t_n)$, respectively, the Crank–Nicolson scheme applied to the above problem reads: starting from $u^0 = v^0 = \lambda^0 = 0$, for $n = 1, \dots, N$,

$$\begin{cases} m(v^n - v^{n-1}, w) + \dfrac{\Delta_t}{2} \alpha m(v^n + v^{n-1}, w) + \dfrac{\Delta_t}{2} c^2 a(u^n + u^{n-1}, w) - \dfrac{\Delta_t}{2} \langle \lambda^n + \lambda^{n-1}, w \rangle = 0, \\ u^n - u^{n-1} = \dfrac{\Delta_t}{2}(v^n + v^{n-1}). \end{cases} \tag{3.1}$$

From the second relation, we get

$$v^n = \frac{2}{\Delta_t}(u^n - u^{n-1}) - v^{n-1}$$

which, inserted in the first relation, leads to

$$\tilde{\alpha} m(u^n, w) + \tilde{c}^2 a(u^n, w) - \frac{\Delta_t^2}{4} \langle \lambda^n, w \rangle = \tilde{\alpha} m(u^{n-1}, w) - \tilde{c}^2 a(u^{n-1}, w) + \Delta_t m(v^{n-1}, w) + \frac{\Delta_t^2}{4} \langle \lambda^{n-1}, w \rangle,$$

where $\tilde{\alpha} := \alpha \frac{\Delta_t}{2} + 1$ and $\tilde{c} := c \frac{\Delta_t}{2}$.

Discretization of the BI-NRBC by the CQ

By collocating the integral relation (2.7c) at the discrete time instant t_n, $n = 1, \dots, N$, we apply the CQ formula and we get

$$\frac{1}{2} u^n(\mathbf{x}) + \sum_{j=1}^{n} \left[\int_\Gamma \omega_{n-j}^V(\mathbf{x}, \mathbf{y}; \Delta_t) \lambda^j(\mathbf{y}) \, \mathrm{d}\Gamma_\mathbf{y} - \int_\Gamma \omega_{n-j}^K(\mathbf{x}, \mathbf{y}; \Delta_t) u^j(\mathbf{y}) \, \mathrm{d}\Gamma_\mathbf{y} \right] = 0, \tag{3.2}$$

where $\omega_j^\mathcal{J}(\mathbf{x}, \mathbf{y}; \Delta_t)$, $\mathcal{J} \in \{V, K\}$, are the convolution weights, whose corresponding integral representations are

$$\omega_j^\mathcal{J}(\mathbf{x}, \mathbf{y}; \Delta_t) := \frac{1}{\imath 2\pi} \int_{|z|=\varrho} \hat{G}^\mathcal{J}\left(\mathbf{x}, \mathbf{y}; \frac{\gamma(z)}{\Delta_t}\right) z^{-j-1} \, \mathrm{d}z. \tag{3.3}$$

In the above equation, $\hat{G}^V := \hat{G}$ and $\hat{G}^K := \widehat{\frac{\partial G}{\partial \mathbf{n}_\mathbf{y}}}$ are the Laplace transforms of the kernels G and $\frac{\partial G}{\partial \mathbf{n}_\mathbf{y}}$ appearing in (2.4) and (2.5), respectively, i.e.

$$\hat{G}^V(\mathbf{x}, \mathbf{y}; s) = \frac{1}{2\pi} K_0\left(\frac{r}{c}\sqrt{s^2 + \alpha s}\right) \quad \text{and} \quad \hat{G}^K(\mathbf{x}, \mathbf{y}; s) = \frac{\sqrt{s^2 + \alpha s}}{2\pi c} \frac{(\mathbf{x} - \mathbf{y}) \cdot \mathbf{n}}{r} K_1\left(\frac{r}{c}\sqrt{s^2 + \alpha s}\right),$$

having denoted by K_0 and K_1 the modified Bessel functions of second kind and orders 0 and 1, respectively, and recalling $r = \|\mathbf{x} - \mathbf{y}\|$. Additionally, in (3.3), $\gamma(z) := \frac{z^2}{2} - 2z + \frac{3}{2}$ represents the characteristic quotient of the Backward Differentiation Formula of order 2 (BDF2), $\imath$ is the imaginary unit and the parameter ϱ is chosen such that the circle $|z| = \varrho$ lies in the domain of analyticity of $\hat{G}^\mathcal{J}(\mathbf{x}, \mathbf{y}; \frac{\gamma(z)}{\Delta_t})$. The convolution weights defined in (3.3) can be approximated numerically, using the L-point trapezoidal rule as follows:

$$\omega_j^\mathcal{J}(\mathbf{x}, \mathbf{y}; \Delta_t) \approx \frac{\varrho^{-j}}{L} \sum_{\ell=0}^{L-1} \hat{G}^\mathcal{J}\left(\mathbf{x}, \mathbf{y}; \frac{\gamma(\varrho e^{\imath \ell \frac{2\pi}{L}})}{\Delta_t}\right) e^{-\imath j \ell \frac{2\pi}{L}}.$$

We choose $L = N$ and $\varrho^N = \varepsilon^{\frac{1}{2}}$ since Lubich has shown in [38] that these values lead to an approximation of $\omega_j^\mathcal{J}$ with relative error of size $\varepsilon^{\frac{1}{2}}$ if $\hat{G}^\mathcal{J}$ is computed with a relative accuracy bounded by ε. In the forthcoming

numerical tests, the parameter ε has been chosen in such a way that the desired accuracy has been reached, in particular $\varepsilon = 10^{-12}$.

All the $\omega_j^{\mathcal{J}}$ can be computed simultaneously by the FFT algorithm, with $\mathcal{O}(N \log N)$ flops, and this represents one of the main benefits of the CQ in terms of its computational cost.

Remark 1. We highlight that, among the most commonly used A-stable ODE solvers of second order, the trapezoidal rule can be considered as an alternative to BDF2 (see, for example, [8, 25]). To apply this solver, it is sufficient to replace the characteristic quotient in formula (3.3) with $\gamma(z) = 2(1-z)(1+z)^{-1}$. In all the numerical tests we have performed, these two methods have given very similar results. In particular, we point out that both the above mentioned ODE solvers guarantee a quadratic convergence order in time (see [38]).

4 Discretization in Space

We introduce a family of meshes $\{\mathcal{T}_{h_\Omega}\}_{h_\Omega}$ of Ω, each consisting of general elements E, whose boundaries $\partial E = e_1 \cup \cdots \cup e_{n_E}$, for simplicity of the presentation, have at most one curved edge, the latter lying either on the physical boundary Γ_0 or on the artificial one, Γ. In particular, we identify the curved edge by e_1, to which we associate a regular invertible parametrization $\gamma_{e_1} : I_{e_1} \to e_1$, where $I_{e_1} \subset \mathbf{R}$ is a closed interval. Furthermore, as typical in the VEM literature, we suppose that there exists a constant $\eta > 0$ such that each E, having diameter h_E, is star-shaped with respect to a ball of radius larger than ηh_E and the length of any (eventually curved) edge of E is larger than ηh_E. The mesh parameter h_Ω corresponds to the largest h_E. We remark that the CVEM allows us to avoid approximation of the geometry; indeed, for each tessellation $\mathcal{T}_{h_\Omega}$, it holds $\overline{\Omega} = \bigcup_{E \in \mathcal{T}_{h_\Omega}} E$. Finally, in order to fully decouple the approximation in space of the interior CVEM with that of the BEM, we denote by $\mathcal{T}_{h_\Gamma}$ a decomposition of the artificial boundary Γ, which consists of a finite number M_Γ of curvilinear parts joined with continuity, of maximum edge size h_Γ.

Discretization of the Variational Problem by the CVEM

We briefly recall the main features of the CVEM which are useful for the description of the space discretization of equation (3.1). The reader is referred to the seminal papers [1, 11, 12, 15] for a thorough description.

Let $E \in \mathcal{T}_{h_\Omega}$ and denote by $\mathcal{P}_{k_\Omega}(E)$ the space of polynomials on E up to degree k_Ω. A basis $\mathcal{M}_{k_\Omega}(E)$ for the space $\mathcal{P}_{k_\Omega}(E)$, particularly suited for the computation of the integrals involved in the numerical calculations (see [12, 21]), consists of scaled monomials on E, i.e.

$$\mathcal{M}_{k_\Omega}(E) := \left\{ m_{\boldsymbol{\alpha}}(\mathbf{x}) = \left(\frac{x_1 - x_1^E}{h_E}\right)^{\alpha_1} \left(\frac{x_2 - x_2^E}{h_E}\right)^{\alpha_2},\ \boldsymbol{\alpha} = (\alpha_1, \alpha_2) : |\boldsymbol{\alpha}| = \alpha_1 + \alpha_2 \le k_\Omega \right\},$$

where $\mathbf{x}^E = (x_1^E, x_2^E)$ denotes the mass center of E.

We define the H^1-projection operator $\Pi_{k_\Omega}^{\nabla,E} : H^1(E) \to P_{k_\Omega}(E)$ such that

$$\begin{cases} \displaystyle\int_E \nabla \Pi_{k_\Omega}^{\nabla,E} v(\mathbf{x}) \cdot \nabla p(\mathbf{x})\, \mathrm{d}\mathbf{x} = \int_E \nabla v(\mathbf{x}) \cdot \nabla p(\mathbf{x})\, \mathrm{d}\mathbf{x} \quad \text{for all } p \in \mathcal{P}_{k_\Omega}(E), \\ \displaystyle\int_{\partial E} \Pi_{k_\Omega}^{\nabla,E} v(\mathbf{x})\, \mathrm{d}s(\mathbf{x}) = \int_{\partial E} v(\mathbf{x})\, \mathrm{d}s(\mathbf{x}), \end{cases}$$

and the L^2-projector $\Pi_{k_\Omega}^{0,E} : L^2(E) \to \mathcal{P}_{k_\Omega}(E)$ such that

$$\int_E \Pi_{k_\Omega}^{0,E} v(\mathbf{x}) p(\mathbf{x})\, \mathrm{d}\mathbf{x} = \int_E v(\mathbf{x}) p(\mathbf{x})\, \mathrm{d}\mathbf{x} \quad \text{for all } p \in \mathcal{P}_{k_\Omega}(E).$$

Since the local CVEM spaces contain not explicitly known functions, the above projectors $\Pi_{k_\Omega}^{\nabla,E}$ and $\Pi_{k_\Omega}^{0,E}$ are needed to compute in practice the contribution of non-polynomial functions to the local stiffness and mass

matrices, respectively. Before defining the CVEM space we will work with, we start by introducing the local finite-dimensional space

$$\tilde{V}_{h_\Omega}^{k_\Omega}(E) := \{v_{h_\Omega} \in H^1(E) : \Delta v_{h_\Omega} \in \mathcal{P}_{k_\Omega-2}(E),\ v_{h_\Omega}|_{e_1} \in \tilde{\mathcal{P}}_{k_\Omega}(e_1),\ v_{h_\Omega}|_{e_i} \in \mathcal{P}_{k_\Omega}(e_i) \text{ for all } i = 2, \dots, n_E\},$$

where $\tilde{\mathcal{P}}_{k_\Omega}(e_1) := \{\tilde{p} = p \circ \gamma_{e_1}^{-1} : p \in \mathcal{P}_{k_\Omega}(I_{e_1})\}$ and $\mathcal{P}_{-1}(E) := \{0\}$. We remark that this space was originally introduced in [11] (for the standard polygonal VEM) and in [15] (for the curved VEM), where the authors considered Poisson problems. In these two papers, it has been shown that the following degrees of freedom are unisolvent for $v_{h_\Omega} \in \tilde{V}_{h_\Omega}^{k_\Omega}(E)$:

- the values at the vertices of E;
- the values at the $k_\Omega - 1$ internal points of the $(k_\Omega + 1)$-point Gauss–Lobatto quadrature rule on each straight edge of ∂E;
- the values at the $k_\Omega - 1$ internal points of the curved edge of ∂E, that are the images through the parametrization γ_{e_1} of the $(k_\Omega + 1)$-point Gauss–Lobatto quadrature rule on the parametric interval I_{e_1};
- the moments up to the order $k_\Omega - 2$,

$$\frac{1}{|E|}\int_E v_{h_\Omega}(\mathbf{x})p(\mathbf{x})\,d\mathbf{x} \quad \text{for all } p \in \mathcal{M}_{k_\Omega-2}(E),$$

where $|E|$ denotes the Lebesgue measure of E. According to the above listed degrees of freedom, for each $v_{h_\Omega} \in \tilde{V}_{h_\Omega}^{k_\Omega}(E)$ the projector $\Pi_{k_\Omega}^{\nabla,E} v_{h_\Omega}$ is computable since, by using Green's formula, we have, for all $p \in \mathcal{P}_{k_\Omega}(E)$,

$$\int_E \nabla\Pi_{k_\Omega}^{\nabla,E} v_{h_\Omega}(\mathbf{x}) \cdot \nabla p(\mathbf{x})\,d\mathbf{x} = \int_E \nabla v_{h_\Omega}(\mathbf{x}) \cdot \nabla p(\mathbf{x})\,d\mathbf{x} = -\int_E \Delta p(\mathbf{x}) v_{h_\Omega}(\mathbf{x})\,d\mathbf{x} + \int_{\partial E} \frac{\partial p}{\partial \mathbf{n}}(\mathbf{x}) v_{h_\Omega}(\mathbf{x})\,ds(\mathbf{x}).$$

It then turns out that, for the standard Poisson problems, the explicit knowledge of the projector $\Pi_{k_\Omega}^{\nabla,E}$ is enough to complete the discretization process and to perform the analysis. Furthermore, by using the moments up to the order $k_\Omega - 2$, we are also able to compute $\Pi_{k_\Omega-2}^{0,E} v_{h_\Omega}$. However, in more general cases like ours, due to the presence of a mass term, it is necessary to have an explicit knowledge, together with $\Pi_{k_\Omega}^{\nabla,E}$ also of the projector $\Pi_{k_\Omega}^{0,E}$. For this reason, we introduce the space

$$\begin{aligned} V_{h_\Omega}^{k_\Omega}(E) := \{v_{h_\Omega} \in H^1(E) : \Delta v_{h_\Omega} \in \mathcal{P}_{k_\Omega}(E),\ v_{h_\Omega}|_{e_1} \in \tilde{\mathcal{P}}_{k_\Omega}(e_1),\ v_{h_\Omega}|_{e_i} \in \mathcal{P}_{k_\Omega}(e_i) \text{ for all } i = 2, \dots, n_E,\\ (\Pi_{k_\Omega}^{\nabla,E} v_{h_\Omega} - \Pi_{k_\Omega}^{0,E} v_{h_\Omega}) \in \mathcal{P}_{k_\Omega-2}(E)\}, \end{aligned}$$

that, as shown in [1], shares with $\tilde{V}_{h_\Omega}^{k_\Omega}(E)$ the same degrees of freedom and allows for the computation of $\Pi_{k_\Omega}^{0,E}$. This latter is the space we will use to define our generalized Galerkin method. To this end, setting $M_\Omega^E := \dim(V_{h_\Omega}^{k_\Omega}(E))$ and choosing an arbitrary but fixed ordering of the degrees of freedom, we define the operators $\mathrm{dof}_i : V_{h_\Omega}^{k_\Omega}(E) \to \mathbf{R}$ such that

$$\mathrm{dof}_i(v_{h_\Omega}) := \text{the value of the } i\text{-th local degree of freedom of } v_{h_\Omega}, \quad i = 1, \dots, M_\Omega^E,$$

and we introduce the canonical basis functions $\{\Phi_j^E\}_j$ for the space $V_{h_\Omega}^{k_\Omega}(E)$, satisfying the condition

$$\mathrm{dof}_i(\Phi_j^E) = \delta_{ij}, \quad i, j = 1, \dots, M_\Omega^E,$$

δ_{ij} being the Kronecker delta. Consequently, a generic function $v_{h_\Omega} \in V_{h_\Omega}^{k_\Omega}(E)$ can be written by means of the following Lagrange-type interpolation identity:

$$v_{h_\Omega} = \sum_{j=1}^{M_\Omega^E} \mathrm{dof}_j(v_{h_\Omega})\Phi_j^E.$$

From the definition of the spaces $V_{h_\Omega}^{k_\Omega}(E)$, we build the global virtual element spaces $V_{h_\Omega}^{k_\Omega}$ by gluing the local ones, i.e.

$$V_{h_\Omega}^{k_\Omega} := \{v_{h_\Omega} \in H^1(\Omega) : v_{h_\Omega}|_E \in V_{h_\Omega}^{k_\Omega}(E) \text{ for all } E \in \mathcal{T}_{h_\Omega}\},$$

and we define the discrete bilinear forms $a_{h_\Omega}\colon V_{h_\Omega}^{k_\Omega} \times V_{h_\Omega}^{k_\Omega} \to \mathbf{R}$ and $m_{h_\Omega}\colon V_{h_\Omega}^{k_\Omega} \times V_{h_\Omega}^{k_\Omega} \to \mathbf{R}$, counterparts of a and m in (2.6), as

$$a_{h_\Omega}(u_{h_\Omega}, v_{h_\Omega}) := \sum_{E\in\mathcal{T}_{h_\Omega}} a_{h_\Omega}^E(u_{h_\Omega}, v_{h_\Omega}) \quad \text{and} \quad m_{h_\Omega}(u_{h_\Omega}, v_{h_\Omega}) := \sum_{E\in\mathcal{T}_{h_\Omega}} m_{h_\Omega}^E(u_{h_\Omega}, v_{h_\Omega})$$

with

$$a_{h_\Omega}^E(u_{h_\Omega}, v_{h_\Omega}) := a^{\mathrm{E}}(\Pi_{k_\Omega}^{\nabla,E} u_{h_\Omega}, \Pi_{k_\Omega}^{\nabla,E} v_{h_\Omega}) + s^{\mathrm{E}}((I - \Pi_{k_\Omega}^{\nabla,E})u_{h_\Omega}, (I - \Pi_{k_\Omega}^{\nabla,E})v_{h_\Omega}) \tag{4.1}$$

$$m_{h_\Omega}^E(u_{h_\Omega}, v_{h_\Omega}) := m^{\mathrm{E}}(\Pi_{k_\Omega-1}^{0,E} u_{h_\Omega}, \Pi_{k_\Omega-1}^{0,E} v_{h_\Omega}). \tag{4.2}$$

The local bilinear forms $a^E(\cdot,\cdot)$ and $m^E(\cdot,\cdot)$ are the restriction of $a(\cdot,\cdot)$ and $m(\cdot,\cdot)$ to E, respectively, while I denotes the identity operator. We remark that the bilinear form $a_{h_\Omega}^E(\cdot,\cdot)$ consists of two terms: the first one accounts for the consistency with polynomials of degree up to k_Ω, while the second one is a suitable stabilization term added to guarantee the coercivity of the form. A standard choice in VEM literature (see [14] and [15] for the polygonal and the curved versions of VEM, respectively), that we have adopted here, is the *dofi-dofi* stabilization form, defined as

$$s^{\mathrm{E}}((I - \Pi_{k_\Omega}^{\nabla,E})u_{h_\Omega}, (I - \Pi_{k_\Omega}^{\nabla,E})v_{h_\Omega}) := \sum_{j=1}^{M_\Omega^E} \mathrm{dof}_j((I - \Pi_{k_\Omega}^{\nabla,E})u_{h_\Omega})\, \mathrm{dof}_j((I - \Pi_{k_\Omega}^{\nabla,E})v_{h_\Omega}).$$

We stress that, according to the choice of the degrees of freedom of $V_{h_\Omega}^{k_\Omega}(E)$, the local projection operators $\Pi_{k_\Omega}^{\nabla,E}$ and $\Pi_{k_\Omega}^{0,E}$, as well as all the quantities in the right-hand sides of (4.1) and (4.2), are computable.

For what concerns the approximation of the unknown λ, we introduce the boundary element space $X_{h_\Gamma}^{k_\Gamma}$ associated to the partition $\mathcal{T}_{h_\Gamma}$ of the artificial boundary Γ which, for a fixed approximation order k_Γ, is

$$X_{h_\Gamma}^{k_\Gamma} := \{\lambda_{h_\Gamma} \in L^2(\Gamma) : \lambda_{h_\Gamma}|_e \in \tilde{P}_{k_\Gamma}(e) \text{ for all } e \in \mathcal{T}_{h_\Gamma}\}.$$

The generalized Galerkin method applied to (3.1) then reads as follows: starting from $u_{h_\Omega}^0 = v_{h_\Omega}^0 = \lambda_{h_\Gamma}^0 = 0$, for each $n = 1, \dots, N$, find $(u_{h_\Omega}^n, \lambda_{h_\Gamma}^n) \in (V_{h_\Omega}^{k_\Omega} \cap H^1_{g(t_n),\Gamma_0}(\Omega)) \times X_{h_\Gamma}^{k_\Gamma}$ such that, for all $w_{h_\Omega} \in (V_{h_\Omega}^{k_\Omega} \cap H^1_{0,\Gamma_0}(\Omega))$,

$$\begin{aligned} &\tilde{\alpha} m_{h_\Omega}(u_{h_\Omega}^n, w_{h_\Omega}) + \tilde{c}^2 a_{h_\Omega}(u_{h_\Omega}^n, w_{h_\Omega}) - \frac{\Delta_t^2}{4}\langle \lambda_{h_\Gamma}^n, w_{h_\Omega}\rangle \\ &\quad = \tilde{\alpha} m_{h_\Omega}(u_{h_\Omega}^{n-1}, w_{h_\Omega}) - \tilde{c}^2 a_{h_\Omega}(u_{h_\Omega}^{n-1}, w_{h_\Omega}) + \Delta_t m_{h_\Omega}(v_{h_\Omega}^{n-1}, w_{h_\Omega}) + \frac{\Delta_t^2}{4}\langle \lambda_{h_\Gamma}^{n-1}, w_{h_\Omega}\rangle, \end{aligned} \tag{4.3}$$

and then update

$$v_{h_\Omega}^n = \frac{2}{\Delta_t}(u_{h_\Omega}^n - u_{h_\Omega}^{n-1}) - v_{h_\Omega}^{n-1}.$$

Remark 2. We have focused on problems set in homogeneous domains, even if in principle the CVEM discretization can be extended to inhomogeneous ones. The treatment of non-constant coefficients would imply non-trivial modifications in the numerical scheme, in particular for what concerns the approximation of the bilinear forms m_{h_Ω} and a_{h_Ω}. We dealt with such issue in [23] for a CVEM-BEM coupling applied to exterior Helmholtz problems with space dependent wave numbers, and we refer the reader to [13], where the polygonal version of the VEM for general second-order elliptic problems was considered.

Discretization of the BI-NRBC by the Collocation BEM

For the discretization in space of the BI-NRBC (3.2), we employ a standard collocation method at the collocation points $\{\mathbf{x}_\kappa\}_{\kappa=1}^{k_\Gamma M_\Gamma} \subset \Gamma$. To detail the computation of the integrals therein involved, we start by splitting the integral on the whole Γ into the sum of the contributions associated to each boundary edge Γ_ℓ in $\mathcal{T}_{h_\Gamma}$,

$$\frac{1}{2}u^n(\mathbf{x}) + \sum_{j=1}^{n}\left[\sum_{\ell=1}^{M_\Gamma}\int_{\Gamma_\ell} \omega_{n-j}^V(\mathbf{x},\mathbf{y};\Delta_t)\lambda^j(\mathbf{y})\,\mathrm{d}\Gamma_\mathbf{y} - \sum_{\ell=1}^{M_\Gamma}\int_{\Gamma_\ell} \omega_{n-j}^K(\mathbf{x},\mathbf{y};\Delta_t)u^j(\mathbf{y})\,\mathrm{d}\Gamma_\mathbf{y}\right] = 0$$

for $\ell = 1, \dots, M_\Gamma$. Then, by introducing for each ℓ the corresponding parametrization $\gamma_\ell \colon I_\ell \to \Gamma_\ell$, we reduce the integration over Γ_ℓ to that over the parametric interval I_ℓ,

$$\frac{1}{2}u^n(\mathbf{x}_\kappa) + \sum_{j=1}^{n}\Bigg[\sum_{\ell=1}^{M_\Gamma}\int_{I_\ell}\omega^V_{n-j}(\mathbf{x}_\kappa, \gamma_\ell(\sigma); \Delta_t)\lambda^j(\gamma_\ell(\sigma))\|\gamma'_\ell(\sigma)\|\,\mathrm{d}\sigma - \sum_{\ell=1}^{M_\Gamma}\int_{I_\ell}\omega^K_{n-j}(\mathbf{x}_\kappa, \gamma_\ell(\sigma); \Delta_t)u^j(\gamma_\ell(\sigma))\|\gamma'_\ell(\sigma)\|\,\mathrm{d}\sigma\Bigg] = 0 \tag{4.4}$$

for $\kappa \in \tilde{\mathcal{S}}_\Gamma := \{1, \dots, k_\Gamma M_\Gamma\}$.

5 Algebraic Formulation of the Fully Discrete Problem

To describe the algebraic formulation of the global scheme, we denote by $\{\Phi^\Omega_i\}_{i\in\mathcal{S}}$ the set of the basis functions of the virtual element space $V^{k_\Omega}_{h_\Omega}$ defined on the tessellation $\mathcal{T}_{h_\Omega}$. For what follows, it is convenient to split the complete index set $\mathcal{S}$ in three subsets $\mathcal{S}_\Omega$, $\mathcal{S}_{\Gamma_0}$ and $\mathcal{S}_\Gamma$: the former is related to the internal degrees of freedom, while the second and the third ones collect those lying on Γ_0 and Γ, respectively. Taking into account the degrees of freedom associated with Γ_0, where we have imposed the Dirichlet datum in a strong form, we decompose the approximation as follows:

$$u^n(\mathbf{x}) \approx u^n_{h_\Omega}(\mathbf{x}) = \sum_{i\in\mathcal{S}}\mathrm{dof}_i(u^n_{h_\Omega})\Phi^\Omega_i(\mathbf{x}) = \sum_{i\in\mathcal{S}_\Omega}u^n_{\Omega,i}\Phi^\Omega_i(\mathbf{x}) + \sum_{i\in\mathcal{S}_\Gamma}u^n_{\Gamma,i}\Phi^\Omega_i(\mathbf{x}) + \sum_{i\in\mathcal{S}_{\Gamma_0}}\mathrm{dof}_i(g(\cdot\,; t_n))\Phi^\Omega_i(\mathbf{x}), \tag{5.1}$$

in terms of the unknowns $\mathbf{u}^n := [u^n_i] \in \mathbf{R}^{|\mathcal{S}_\Omega\cup\mathcal{S}_\Gamma|}$, split as $\mathbf{u}^n = [\mathbf{u}^n_\Omega\ \mathbf{u}^n_\Gamma]$, with obvious meaning of the underscript notation.

Moreover, we introduce a set $\{\Psi^\Gamma_i\}_{i\in\tilde{\mathcal{S}}_\Gamma}$ of basis functions for the boundary element space $X^{k_\Gamma}_{h_\Gamma}$ so that we write

$$\lambda^n(\mathbf{x}) \approx \lambda^n_{h_\Gamma}(\mathbf{x}) = \sum_{i\in\tilde{\mathcal{S}}_\Gamma}\lambda^n_i\Psi^\Gamma_i(\mathbf{x}) \tag{5.2}$$

in terms of the unknowns $\boldsymbol{\lambda}^n := [\lambda^n_i] \in \mathbf{R}^{|\tilde{\mathcal{S}}_\Gamma|}$. Hence, inserting relations (5.1) (as well as the analogous for $v^n_{h_\Omega}$) and (5.2) into the fully discrete problem (4.3), we get

$$[\tilde{\alpha}\mathbb{M} + \tilde{c}^2\mathbb{A}]\mathbf{u}^n - \frac{\Delta_t^2}{4}\mathbb{Q}\boldsymbol{\lambda}^n = [\tilde{\alpha}\mathbb{M} - \tilde{c}^2\mathbb{A}]\mathbf{u}^{n-1} + \Delta_t\mathbb{M}\mathbf{v}^{n-1} + \frac{\Delta_t^2}{4}\mathbb{Q}\boldsymbol{\lambda}^{n-1} \tag{5.3}$$

for each $n = 1, \dots, N$. In the above equation, we have introduced the mass matrix $\mathbb{M}$, the stiffness matrix $\mathbb{A}$ and the matrix $\mathbb{Q}$, whose entries are respectively defined by

$$\mathbb{M}_{i_1 i_2} := m_{h_\Omega}(\Phi^\Omega_{i_2}, \Phi^\Omega_{i_1}) \quad \text{and} \quad \mathbb{A}_{i_1 i_2} := a_{h_\Omega}(\Phi^\Omega_{i_2}, \Phi^\Omega_{i_1}), \quad \mathbb{Q}_{i_3 i_4} := \langle\Psi^\Gamma_{i_4}, \Phi^\Omega_{i_3}\rangle,$$

with $i_1, i_2 \in \mathcal{S}_\Omega \cup \mathcal{S}_\Gamma$, $i_3 \in \mathcal{S}_\Gamma$ and $i_4 \in \tilde{\mathcal{S}}_\Gamma$.

To obtain the matrix form of the BI-NRBC, we insert relations (5.1) and (5.2) into the fully discrete equation (4.4), and we get, for $n = 1, \dots, N$ and $\kappa = 1, \dots, k_\Gamma M_\Gamma$,

$$\frac{1}{2}\sum_{i\in\mathcal{S}_\Gamma}u^n_{\Gamma,i}\Phi^\Omega_i(\mathbf{x}_\kappa) + \sum_{j=1}^{n}\Bigg[\sum_{i\in\tilde{\mathcal{S}}_\Gamma}\lambda^j_i\sum_{\ell=1}^{M_\Gamma}\int_{I_\ell}\omega^V_{n-j}(\mathbf{x}_\kappa, \gamma_\ell(\sigma); \Delta_t)\Psi^\Gamma_i(\gamma_\ell(\sigma))\|\gamma'_\ell(\sigma)\|\,\mathrm{d}\sigma - \sum_{i\in\mathcal{S}_\Gamma}u^j_{\Gamma,i}\sum_{\ell=1}^{M_\Gamma}\int_{I_\ell}\omega^K_{n-j}(\mathbf{x}_\kappa, \gamma_\ell(\sigma); \Delta_t)\Phi^\Omega_i(\gamma_\ell(\sigma))\|\gamma'_\ell(\sigma)\|\,\mathrm{d}\sigma\Bigg] = 0.$$

Introducing the matrices $\mathbb{V}$, $\mathbb{K}$ and $\mathbb{N}$, whose entries are, respectively, for $j = 1, \dots, N$,

$$\mathbb{V}^j_{i_1 i_2} := \sum_{\ell=1}^{M_\Gamma}\int_{I_\ell}\omega^V_j(\mathbf{x}_{i_1}, \gamma_\ell(\sigma); \Delta_t)\Psi^\Gamma_{i_2}(\gamma_\ell(\sigma))\,\|\gamma'_\ell(\sigma)\|\,\mathrm{d}\sigma, \quad i_1, i_2 \in \tilde{S}_\Gamma,$$

$$\mathbb{K}^j_{i_1 i_2} := \sum_{\ell=1}^{M_\Gamma} \int_{I_\ell} \omega_j^K(\mathbf{x}_{i_1}, \gamma_\ell(\sigma); \Delta_t) \Phi^\Omega_{i_2}(\gamma_\ell(\sigma)) \|\gamma'_\ell(\sigma)\| \, \mathrm{d}\sigma, \quad i_1 \in \tilde{S}_\Gamma,\ i_2 \in S_\Gamma,$$

$$\mathbb{N}_{i_1 i_2} := \Phi^\Omega_{i_2}(\mathbf{x}_{i_1}), \quad i_1 \in \tilde{S}_\Gamma,\ i_2 \in S_\Gamma,$$

the final matrix form of the BI-NRBC reads

$$\left(\frac{1}{2}\mathbb{N} - \mathbb{K}^0\right)\mathbf{u}^n_\Gamma + \mathbb{V}^0 \boldsymbol{\lambda}^n = \sum_{j=1}^{n-1} \mathbb{K}^{n-j}\mathbf{u}^j_\Gamma - \sum_{j=1}^{n-1} \mathbb{V}^{n-j}\boldsymbol{\lambda}^j, \quad n = 1, \dots, N. \tag{5.4}$$

According to the partitioning of the index set $\mathcal{S}$, previously introduced, $\mathbb{M}$ and $\mathbb{A}$ can be decomposed in the following block structures:

$$\mathbb{M} = \begin{bmatrix} \mathbb{M}_{\Omega\Omega} & \mathbb{M}_{\Omega\Gamma} \\ \mathbb{M}_{\Gamma\Omega} & \mathbb{M}_{\Gamma\Gamma} \end{bmatrix}, \quad \mathbb{A} = \begin{bmatrix} \mathbb{A}_{\Omega\Omega} & \mathbb{A}_{\Omega\Gamma} \\ \mathbb{A}_{\Gamma\Omega} & \mathbb{A}_{\Gamma\Gamma} \end{bmatrix}.$$

Finally, starting from $\mathbf{u}^0_\Omega = \mathbf{u}^0_\Gamma = \boldsymbol{\lambda}^0 = \mathbf{0}$ and coupling equations (5.3) and (5.4), for each $n = 1, \dots, N$, we solve the global linear system

$$\begin{bmatrix} \tilde{\alpha}\mathbb{M}_{\Omega\Omega} + \tilde{c}^2\mathbb{A}_{\Omega\Omega} & \tilde{\alpha}\mathbb{M}_{\Omega\Gamma} + \tilde{c}^2\mathbb{A}_{\Omega\Gamma} & \mathbb{O} \\ \tilde{\alpha}\mathbb{M}_{\Gamma\Omega} + \tilde{c}^2\mathbb{A}_{\Gamma\Omega} & \tilde{\alpha}\mathbb{M}_{\Gamma\Gamma} + \tilde{c}^2\mathbb{A}_{\Gamma\Gamma} & -\frac{\Delta_t^2}{4}\mathbb{Q} \\ \mathbb{O} & \frac{1}{2}\mathbb{N} - \mathbb{K}^0 & \mathbb{V}^0 \end{bmatrix} \begin{bmatrix} \mathbf{u}^n_\Omega \\ \mathbf{u}^n_\Gamma \\ \boldsymbol{\lambda}^n \end{bmatrix}$$

$$= \begin{bmatrix} [\tilde{\alpha}\mathbb{M}_{\Omega\Omega} - \tilde{c}^2\mathbb{A}_{\Omega\Omega}]\mathbf{u}^{n-1}_\Omega + [\tilde{\alpha}\mathbb{M}_{\Omega\Gamma} - \tilde{c}^2\mathbb{A}_{\Omega\Gamma}]\mathbf{u}^{n-1}_\Gamma + \Delta_t\mathbb{M}_{\Omega\Omega}\mathbf{v}^{n-1}_\Omega + \Delta_t\mathbb{M}_{\Omega\Gamma}\mathbf{v}^{n-1}_\Gamma \\ [\tilde{\alpha}\mathbb{M}_{\Gamma\Omega} - \tilde{c}^2\mathbb{A}_{\Gamma\Omega}]\mathbf{u}^{n-1}_\Omega + [\tilde{\alpha}\mathbb{M}_{\Gamma\Gamma} - \tilde{c}^2\mathbb{A}_{\Gamma\Gamma}]\mathbf{u}^{n-1}_\Gamma + \Delta_t\mathbb{M}_{\Gamma\Omega}\mathbf{v}^{n-1}_\Omega + \Delta_t\mathbb{M}_{\Gamma\Gamma}\mathbf{v}^{n-1}_\Gamma + \frac{\Delta_t^2}{4}\mathbb{Q}\boldsymbol{\lambda}^{n-1} \\ \sum_{j=1}^{n-1}\mathbb{K}^{n-j}\mathbf{u}^j_\Gamma - \sum_{j=1}^{n-1}\mathbb{V}^{n-j}\boldsymbol{\lambda}^j \end{bmatrix}$$

and update

$$\mathbf{v}^n = \frac{2}{\Delta_t}(\mathbf{u}^n - \mathbf{u}^{n-1}) - \mathbf{v}^{n-1}.$$

Remark 3. For the accuracy of the global scheme, it is crucial to compute the integrals defining the BEM matrix elements with a high precision. The numerical integration difficulties are due to the logarithmic asymptotic behavior of the Bessel function $K_0(r)$ near the origin, the latter being the Laplace transform of the kernel in the single-layer operator V. In particular, these are associated to the entries of the matrix $\mathbb{V}$ belonging to the main diagonal and to the co-diagonals, for which the collocation points belong or are close to the supports of the basis functions. For their accurate computation by a few nodes, we have used the very simple and efficient polynomial smoothing transformation proposed in [39], referred to as the *q-smoothing* technique. After having introduced the *q-smoothing* transformation, with $q = 3$, we have applied the ν-point Gauss–Legendre quadrature rule with $\nu = 16$. For the computation of all the other integrals, we have applied a standard 8-point Gauss–Legendre quadrature rule. Finally, we point out that the integrals involving the Bessel function $K_1(r)$, appearing in the Laplace transform of the kernel of the double layer operator K, do not require a particular quadrature strategy since its singularity $\frac{1}{r}$ is factored out by the same behavior of $\frac{\partial r}{\partial \mathbf{n}}$ near the origin (see [28]). Hence, for the computation of the entries of the matrix $\mathbb{K}$, we have directly applied a standard 8-point Gauss–Legendre quadrature rule. The above described quadrature strategy has guaranteed the computation of all the mentioned integrals with high accuracy for both $k_\Gamma = 1$ and $k_\Gamma = 2$.

6 Numerical Results

In this section we show the effectiveness of the proposed approach, presenting four examples selected in our extensive numerical testing, and we highlight its competitiveness by applying it to some problems from the literature.

We organize this section as follows. In the first example, we provide a numerical convergence study by applying the proposed method to a benchmark problem both for the classical wave equation and for the damped

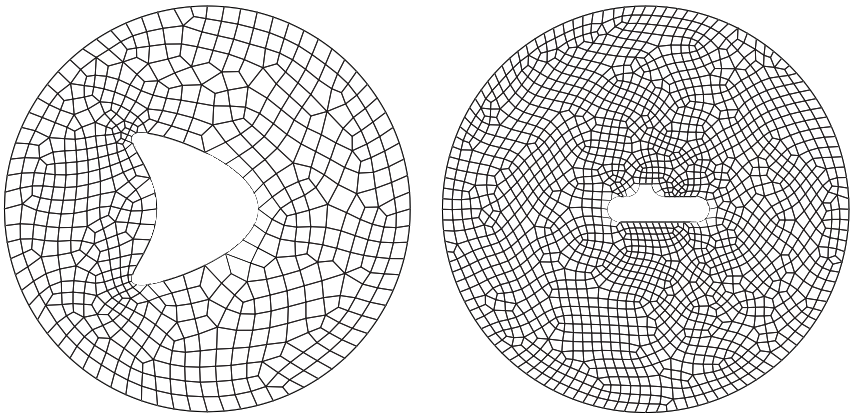

Figure 1: Two representative meshes for complex geometries: on the left for a kite-shaped scatterer (Example 2), on the right for a simplified submarine obstacle (Example 3).

one. In Examples 2 and 3, we deal with complex curved geometries and we compare our numerical results with some present in literature, showing the performance of our method applied to real life applications. In the last test, we consider a multiple obstacle scattering problem and we solve it by means of a CVEM-BEM coupling with decoupled orders for the interior and the boundary discretizations.

In all the reported numerical tests, we have used the GMSH software (see [32]) to construct unstructured conforming polygonal CVEM meshes $\{\mathcal{T}_{h_\Omega}\}_{h_\Omega}$. To generate curvilinear edges, those bordering with the interior boundary Γ_0 or with the artificial one Γ, we transform the associated straight ones into curved edges by means of the corresponding parametrizations (see Figure 1 for two representative meshes). Even if in principle it is possible to fully decouple the interior and boundary elements, both for the choice of the approximation orders and for that of the meshes, for simplicity, we consider the boundary meshes $\{\mathcal{T}_{h_\Gamma}\}_{h_\Gamma}$ inherited by the interior ones.

All the numerical computations have been performed on a cluster with dual socket Intel Xeon Skylake Gold 6130 (2.1 GHz clock frequency, 16 cores, 22 MB L3 cache) and 192 GB RAM (DDR4 2666 MHz with ECC) by means of parallel Matlab® codes.

Example 1

Let Ω_e be the unbounded region, external to the unitary disk $\Omega_0 = \{\mathbf{x} = (x_1, x_2) \in \mathbf{R}^2 : x_1^2 + x_2^2 \leq 1\}$. We consider equation (2.1) with $c \in \{1, 343\}$, $\alpha \in \{0, 10\}$ and the Dirichlet datum $g(\mathbf{x}; t) = t^3 e^{-t} \cos(x_1 + 2x_2^2)$, prescribed on the boundary $\Gamma_0 = \partial\Omega_0$. We choose as artificial boundary Γ the circumference of radius 2 so that the finite computational domain Ω is the annulus bounded internally by Γ_0 and externally by Γ.

To develop a convergence analysis, we start by choosing a coarse mesh, associated to the level of refinement zero (referred to as lev. 0), and all the successive refinements are obtained by halving each side of its elements. Based on the analysis performed in [22, 23] for the Helmholtz and Poisson problems, and recalling that we are applying second-order methods in time, we expect that, for a sufficiently smooth solution u, the $L^2(\Omega)$-norm and $H^1(\Omega)$-seminorm errors behave like

$$\max_{n=0,\dots,N} |u(\cdot; t_n) - u^n_{h_\Omega}|_{H^1(\Omega)} = \mathcal{O}(h_\Omega^{k_\Omega} + h_\Gamma^{k_\Gamma+1} + \Delta_t^2), \tag{6.1}$$

$$\max_{n=0,\dots,N} \|u(\cdot; t_n) - u^n_{h_\Omega}\|_{L^2(\Omega)} = \mathcal{O}(h_\Omega^{k_\Omega+1} + h_\Gamma^{k_\Gamma+2} + \Delta_t^2). \tag{6.2}$$

To test our numerical approach, the order k_Ω of the approximation spaces is chosen equal to 1 (linear) and 2 (quadratic), and $k_\Gamma = k_\Omega$. Moreover, since the exact solution u is not explicitly known, we compare the approximations with a reference one denoted by $u_{\tilde{h}_\Omega,\tilde{N}}$, which is obtained with a sufficiently fine space and time refinements (Figure 2). In particular, in Tables 1, 2 and 3, $u_{\tilde{h}_\Omega,\tilde{N}}$ is obtained with the space refinement lev. 5, for which $\tilde{h}_\Omega = 2.84\text{e}{-02}$, and with a proper $\tilde{N}$ which is specified in the corresponding captions. Due to the limi-

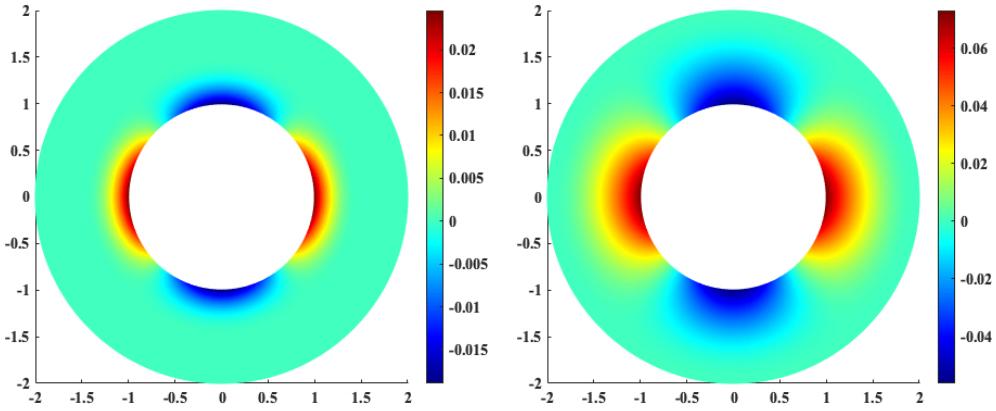

Figure 2: Example 1. Reference solution at the time instants $t = \frac{1}{2}$ (left plot) and $t = 1$ (right plot).

tations of the hardware used for our simulations, we were not able to compute the reference solution with finer space-time refinements. However, the observed error behavior seems to confirm the theoretical expected one.

Recalling that both the approximate and reference solutions are not known inside the elements, we estimate the absolute errors and the corresponding Estimated Order of Convergence (EOC) by means of the following computable formulas:

$$
\begin{aligned}
H^1(\Omega)\text{-seminorm:} \quad & \varepsilon^{\nabla,k_\Omega}_{\mathrm{lev},n} := \sqrt{\sum_{E\in\mathcal{T}_{h_\Omega}} |\Pi^{\nabla,E}_{k_\Omega} u^n_{\tilde{h}_\Omega,\tilde{N}} - \Pi^{\nabla,E}_{k_\Omega} u^n_{h_\Omega}|^2_{H^1(E)}}, \\
L^2(\Omega)\text{-norm:} \quad & \varepsilon^{0,k_\Omega}_{\mathrm{lev},n} := \sqrt{\sum_{E\in\mathcal{T}_{h_\Omega}} \|\Pi^{0,E}_{k_\Omega} u^n_{\tilde{h}_\Omega,\tilde{N}} - \Pi^{0,E}_{k_\Omega} u^n_{h_\Omega}\|^2_{L^2(E)}}, \\
& \mathrm{EOC} := \log_2\left(\frac{\varepsilon^{*,k_\Omega}_{\mathrm{lev}+1,n}}{\varepsilon^{*,k_\Omega}_{\mathrm{lev},n}}\right), \quad * = \nabla, 0.
\end{aligned}
$$

This is a natural choice, justified by the following estimate, easily derived from classical results concerning VEM (see, for example, [17]):

$$
\begin{aligned}
|\Pi^{\nabla,E}_{k_\Omega} u^n_{\tilde{h}_\Omega,\tilde{N}} - \Pi^{\nabla,E}_{k_\Omega} u^n_{h_\Omega}|_{H^1(E)} &\le |\Pi^{\nabla,E}_{k_\Omega} u^n_{\tilde{h}_\Omega,\tilde{N}} - u(\cdot;t_n)|_{H^1(E)} + |u(\cdot;t_n) - \Pi^{\nabla,E}_{k_\Omega} u^n_{h_\Omega}|_{H^1(E)} \\
&\le |\Pi^{\nabla,E}_{k_\Omega} u^n_{\tilde{h}_\Omega,\tilde{N}} - u^n_{\tilde{h}_\Omega,\tilde{N}}|_{H^1(E)} + |u^n_{\tilde{h}_\Omega,\tilde{N}} - u(\cdot;t_n)|_{H^1(E)} + |u(\cdot;t_n) - \Pi^{\nabla,E}_{k_\Omega} u^n_{h_\Omega}|_{H^1(E)} \\
&\le C(h^{k_\Omega}_\Omega + \tilde{h}^{k_\Omega}_\Omega)|u(\cdot;t_n)|_{H^{k_\Omega+1}(E)} \le h^{k_\Omega}_\Omega |u(\cdot;t_n)|_{H^{k_\Omega+1}(E)},
\end{aligned}
$$

where C is a constant not depending on h_Ω and h_Γ, and similarly for the L^2-norm.

The above errors are computed using the 8-point quadrature formulas proposed in [42, 43]. For curved polygons, we have applied the generalization of the latter as suggested in [15, Section 4.3].

In Table 1, to show the CVEM-BEM convergence in space, we fix the time discretization by choosing a sufficiently fine Δ_t such that the error depends only on the space discretization. In particular, for the standard wave equation ($\alpha = 0$) with $c = 1$, we report $\varepsilon^{0,k_\Omega}_{\mathrm{lev},N}$, $\varepsilon^{\nabla,k_\Omega}_{\mathrm{lev},N}$ at the final time $t_N = T = 1$ and the corresponding EOC by varying the space mesh refinement from lev. 0 to lev. 4. As we can see, the H^1-seminorm and the L^2-norm error estimates confirm the expected convergence order of the method. In particular, we observe a superconvergence for the H^1-seminorm when using the linear CVEM. This phenomenon has been confirmed by an extensive numerical testing, performed by varying the problem data, the mesh refinements and applying the polygonal version of the VEM instead of curvilinear one. Therefore, it could be ascribed to the regularity of the meshes, the smoothness of the solution and the type of error considered, which involves a reference solution instead of an exact one.

We omit here the results obtained with the coupling $k_\Omega = 2$ and $k_\Gamma = 1$ since they are very similar to those reported in Table 1 for the choice $k_\Omega = k_\Gamma = 2$. This is coherent with formulas (6.1) and (6.2), recalling that the boundary meshes are those inherited from the interior ones, so that $h_\Gamma \le h_\Omega$. We further highlight that we have

		L^2-norm				H^1-seminorm			
lev.	h_Ω	$\varepsilon^{0,1}_{\text{lev},64}$	EOC	$\varepsilon^{0,2}_{\text{lev},400}$	EOC	$\varepsilon^{\nabla,1}_{\text{lev},64}$	EOC	$\varepsilon^{\nabla,2}_{\text{lev},400}$	EOC
0	8.02e−01	1.71e−03		3.02e−03		1.14e−02		2.97e−03	
			1.5		2.9		1.6		2.2
1	4.28e−01	6.66e−04		3.99e−04		4.90e−03		6.38e−04	
			1.6		2.8		1.7		2.4
2	2.22e−01	2.27e−04		5.57e−05		1.77e−03		1.21e−04	
			1.8		2.8		1.6		2.0
3	1.13e−01	6.57e−05		7.99e−06		6.30e−04		3.13e−05	
			2.2		2.8		1.8		2.1
4	5.68e−02	1.05e−05		1.18e−06		9.65e−05		7.54e−06	

Table 1: Example 1. Absolute errors and EOC for $\tilde{N} = N = 64$ when $k_\Omega = k_\Gamma = 1$, and $\tilde{N} = N = 400$ when $k_\Omega = k_\Gamma = 2$.

k_Ω	lev. 0, $N = 32$	lev. 1, $N = 64$	lev. 2, $N = 96$	lev. 3, $N = 128$
1	1.89e−03	9.25e−04	3.09e−04	8.74e−05
2	3.03e−04	5.04e−05	9.90e−05	4.29e−06
3	8.88e−05	3.11e−05	5.15e−05	3.52e−06
4	3.65e−05	1.47e−05	6.31e−06	3.08e−06

Table 2: Example 1. Absolute L^∞ errors on Γ for $\tilde{N} = 400$ and $k_\Gamma = 1$.

$c = 343$, $\alpha = 0$			L^2-norm		H^1-seminorm	
lev.	h_Ω	N	$\varepsilon^{0,1}_{\text{lev},N}$	EOC	$\varepsilon^{\nabla,1}_{\text{lev},N}$	EOC
0	8.02e−01	8	8.96e−04		3.66e−03	
				1.9		1.5
1	4.28e−01	16	2.44e−04		1.31e−03	
				1.9		1.6
2	2.22e−01	32	6.61e−05		4.45e−04	
				2.0		1.7
3	1.13e−01	64	1.66e−05		1.41e−04	
				2.3		2.1
4	5.68e−02	128	3.35e−06		3.38e−05	

$c = 1$, $\alpha = 10$			L^2-norm		H^1-seminorm	
lev.	h_Ω	N	$\varepsilon^{0,1}_{\text{lev},N}$	EOC	$\varepsilon^{\nabla,1}_{\text{lev},N}$	EOC
0	8.02e−01	8	2.42e−03		9.91e−02	
				1.8		1.3
1	4.28e−01	16	7.08e−04		4.07e−03	
				1.9		1.5
2	2.22e−01	32	1.90e−04		1.43e−03	
				2.0		1.6
3	1.13e−01	64	4.70e−05		4.70e−04	
				2.3		1.9
4	5.68e−02	128	9.57e−06		1.30e−05	

Table 3: Example 1. Absolute errors and EOC for $k_\Omega = k_\Gamma = 1$, by varying h_Ω.

built unstructured conforming meshes, by employing the Mesh.ElementOrder option within the GMSH code. In particular, to simplify the creation of the meshes used in this example, we have generated the decomposition of the computational domain in such a way that $h_\Gamma = \frac{h_\Omega}{2}$.

To underline further the advantage of decoupling the interior and boundary orders of accuracy, in Table 2, we show the absolute L^∞ errors on Γ at the final time instant $T = 1$, by fixing $k_\Gamma = 1$ and varying k_Ω. The discretization parameter N has been properly chosen in such a way that the error in time does not affect that in space. As we can see, for a fixed space refinement, the error decreases by increasing k_Ω, and the low-order BEM approximation does not significantly pollute that of the VEM for the refinements levels 0, 1 and 2, while it is (as possibly expected) no more negligible for level 3 by using $k_\Omega = 3, 4$. Therefore, the order decoupling strategy allows to avoid the over-resolution of boundary variables and represents a great gain in terms of computational cost and memory saving since higher-order BEMs are demanding for the efficient computation of the associated matrices.

To show the quadratic convergence order in time stated in estimates (6.1) and (6.2), in Figure 3, we report the H^1-seminorm and L^2-norm errors obtained by fixing the space mesh corresponding to level 3 and by varying the time step Δ_t. We remark that in [9] a theoretical and numerical error analysis has been presented for a similar coupling approach, observing the convergence order $\mathcal{O}(\Delta_t^2)$.

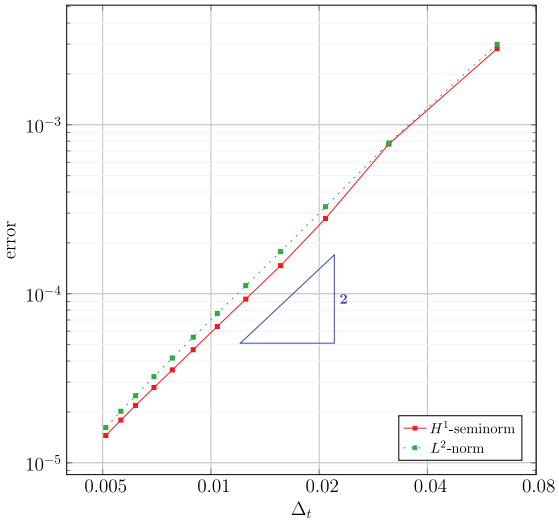

Figure 3: Example 1. H^1-seminorm and L^2-norm convergence errors with respect to the time step Δ_t.

In Table 3, we show the global space-time error behavior. In particular, we report the absolute errors and the corresponding EOC for $T = 1$. These are obtained by choosing $k_\Omega = k_\Gamma = 1$, starting with a fixed mesh in time and in space, and then halving Δ_t and h_Ω at each refinement step. We consider $c = 343$ and $\alpha = 0$ in the left table, and $c = 1$ and $\alpha = 10$ in the right table. Also in these cases, the results are in agreement with estimates (6.1) and (6.2), and we observe a super-convergence in the H^1-seminorm. Finally, we remark that similar results have been obtained for other choices of c and α, but for brevity, we omit them.

Example 2

As second example, we apply the proposed numerical scheme to a problem solved in [19, Section 6.1]. The test aims at simulating the scattering of transient acoustic waves by an infinitely long cylindrical obstacle on a flat sound-soft substrate. The surrounding space consists of a homogeneous medium. Supposing the substrate and the incident field invariant with respect to a fixed direction, the problem is reduced to a two-dimensional one. The incident wave, generated by a causal signal $\lambda(t)$ simultaneously emitted by a line source, takes the form

$$u_{\text{inc}}(\mathbf{x}, \mathbf{y}_s; t) = G(\mathbf{x}, \mathbf{y}_s; t) * \lambda(t), \tag{6.3}$$

where G is the wave equation kernel (see (2.2) with $\alpha = 0$) and $\mathbf{y}_s = (y_{s,1}, y_{s,2}) \in \mathbf{R}^2$ is a point on the line source. The convolution product in (6.3) has been efficiently computed by the CQ, with the same number N of time instants used in the numerical approach of the associated BIE.

In [19], the authors have solved the problem by a BEM in the half-space $x_2 \geq 0$, combining the CQ with a Nyström method in space. Instead, we consider here the wave equation in the full bi-dimensional space for which, taking into account the antisymmetric property of the solution, the boundary datum consists of the sum of two reflected fields,

$$g(\mathbf{x}; t) = -u_{\text{inc}}(\mathbf{x}, \mathbf{y}_s; t) + u_{\text{inc}}(\mathbf{x}, \mathbf{y}_s^\rho; t),$$

where we have denoted $\mathbf{y}_s^\rho = (y_{s,1}, -y_{s,2})$ the reflection of $\mathbf{y}_s$ about the x_1-axis. We remark that the function $-g$ can be regarded as the wave field emitted from the source points $\mathbf{y}_s$ and $\mathbf{y}_s^\rho$: precisely, the points $\mathbf{y}_s$ and $\mathbf{y}_s^\rho$ emit the signals λ and $-\lambda$, respectively.

In our numerical simulation, we have considered $c = 1$ and $\lambda(t) = \sin(4t)e^{1.6(t-3)^2}$. The time interval of interest $[0, 11.2]$ is subdivided into $N = 512$ sub-intervals so that $\Delta_t = 2.2\text{e}{-02}$. The source point is

$$\mathbf{y}_s = \left(4\cos\left(\frac{2\pi}{5}\right), 4\sin\left(\frac{2\pi}{5}\right)\right),$$

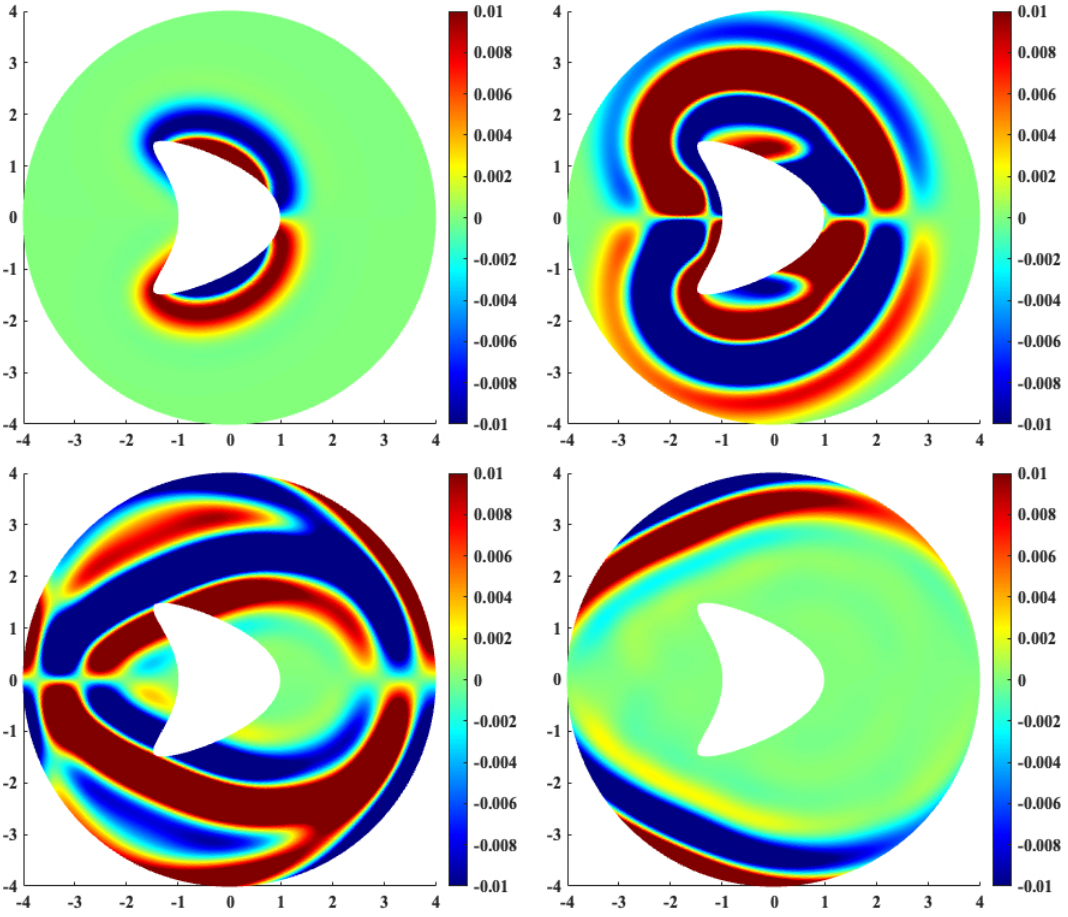

Figure 4: Example 2. Snapshots of the approximate solution at the instants $t \approx 5.9, 7.6, 9.4, 11.1$ (from top left to bottom right).

and the obstacle Ω_0 is a kite-shaped scatterer whose boundary Γ_0 has the following parametrization:

$$\mathbf{q}(\vartheta) = \big(\cos(\vartheta) + 0.65\cos(2\vartheta), 1.5\sin(\vartheta)\big), \quad \vartheta \in (-\pi, \pi].$$

We consider the approximation orders $k_\Omega = k_\Gamma = 1$ and we fix the level of refinement with $h_\Omega = 1.64\text{e}{-01}$ (14,811 degrees of freedom). The snapshots of the scattered field u_{h_Ω} at the time instants $t \approx 5.9, 7.6, 9.4, 11.1$ are shown in Figure 4. By comparing them with those presented in [19, Figures 4 and 5], we observe a qualitative accordance of the solution and that its antisymmetric property is preserved. Moreover, contrary to what is shown in [19], the propagating mode is well approximated by our approach, without the presence of wavy or undulating effects. Indeed, these latter are not expected taking into account the smoothness of the problem data and the geometry regularity of the obstacle.

Example 3

We consider a scattering problem where the incident wave is given by the convolution between the fundamental solution of the wave equation (see (2.2) with $\alpha = 0$) and a time periodic signal, perturbed by a Gaussian spatially distributed source, i.e.

$$u_{\text{inc}}(\mathbf{x}; t) = e^{-\frac{\log 2}{0.04}\|\mathbf{x}-\mathbf{y}_s\|^2} G(\mathbf{x}, \mathbf{y}_s; t) * \sin(8\pi t),$$

where $\mathbf{y}_s = (4, 0)$ is the emission point. The obstacle Ω_0 is a submarine, whose simplified configuration is detailed in [45, Figure 23], the artificial boundary Γ is the circumference of radius 8 and the speed of wave propagation is $c = 1$.

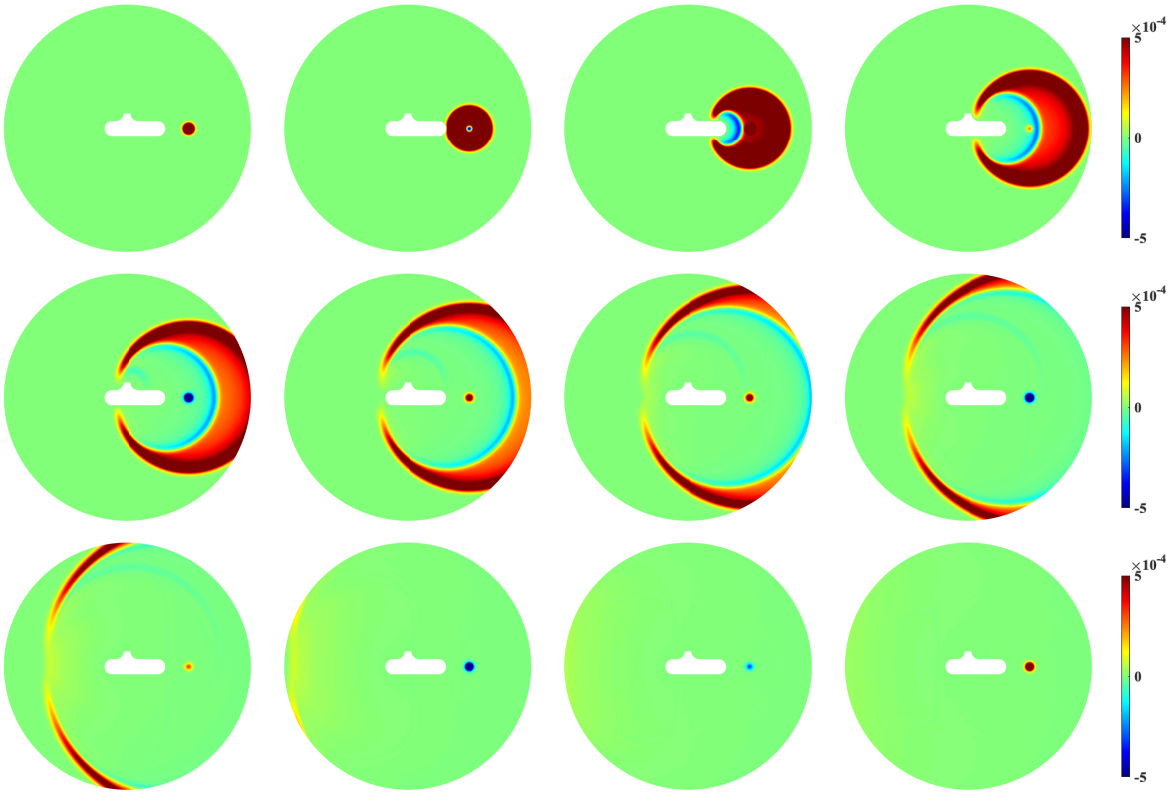

Figure 5: Example 3. Snapshots of the approximate scattered field at the instants (from top left to bottom right) $t_5, t_{45}, t_{85}, t_{125}, t_{165}, t_{205}, t_{245}, t_{285}, t_{325}, t_{365}, t_{405}, t_{445}, t_{485}$.

In Figure 5, we show some snapshots of the scattered field, obtained with the choice $k_\Omega = k_\Gamma = 1$, for a mesh with $h_\Omega = 5.42\text{e}{-02}$ (590,768 degrees of freedom), and by a uniform partitioning of the time interval $[0, 15]$ into 513 instants. As we can see, the scattered field is well approximated by the global scheme and the artificial boundary is perfectly transparent since no pollution effects are present near Γ. In support of this, we compare our solution with that provided by the FEM-BEM coupling. In particular, in the left plot of Figure 6, we report the time history of the scattered fields $u_{h_\Omega}(\hat{\mathbf{x}}; t)$, obtained by both approaches at the fixed point $\hat{\mathbf{x}} = (8, 0) \in \Gamma$. In the right plot, we show the absolute error between the two solutions; as we can see, the maximum gap is of order 1.0e−06, which implies a good agreement of the two approaches and validates the correctness of the scattered field computed by the new proposed strategy.

Example 4

Similarly to [24, Example 3.3], we consider the acoustic field, solution of equation (2.1) with $c = 1$ and $\alpha = 0$, scattered by five obstacles, whose circular sections $\Omega_{0,p}$, $p = 1, \ldots, 5$, are disks of radius $r = 0.3$. The corresponding centers are $\mathbf{O}_1 = (0, 0)$, $\mathbf{O}_2 = (2, 0) = -\mathbf{O}_3$, $\mathbf{O}_4 = (0, 2) = -\mathbf{O}_5$. In this configuration, the reproduction of the scattered field is extremely complex in the region between the obstacles, when these are bumped by incident waves. Aiming at determining an accurate solution in that region, we surround the scatterers by a proper non-convex flower-shaped curve, defined by $\Gamma = \{f(\vartheta)(\cos\vartheta, \sin\vartheta), \vartheta \in (-\pi, \pi]\}$ with $f(\vartheta) = 2.35(1 + 0.7\cos(4\vartheta))$. We consider the Dirichlet datum g defined by the sum of eight plane incident waves, four coming from north east and four coming from south west,

$$g(\mathbf{x}; t) = \sum_{j=1}^{4} e^{-\beta(\mathbf{x}\cdot\mathbf{d}+d_j-t)^2} + \sum_{j=1}^{4} e^{-\beta(\mathbf{x}\cdot\mathbf{d}-d_j+t)^2}$$

with $\beta = 35$, $\mathbf{d} = (1, 1)$ and $d_j = j + 4$ for $j = 1, \ldots, 4$.

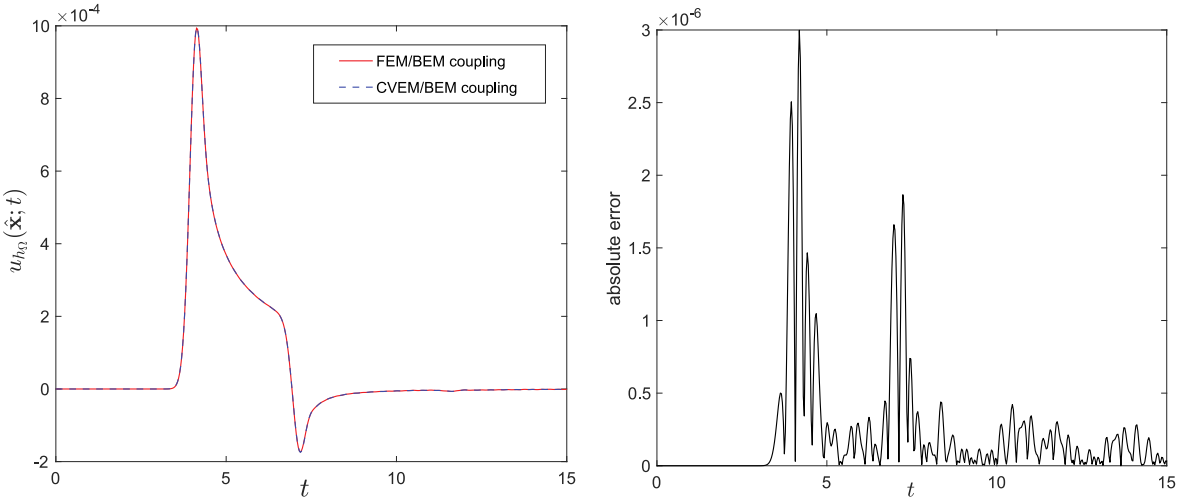

Figure 6: Example 3. Comparison between the FEM-BEM and CVEM-BEM couplings: time history of $u_{h_\Omega}(\hat{\mathbf{x}};t)$, with $\hat{\mathbf{x}} = (8,0) \in \Gamma$ (left plot) and the corresponding absolute error (right plot).

The computational domain has been decomposed into 4,580 quadrilaterals, with mesh size $h_\Omega = 1.80\text{e}{-01}$, and the discrete solution has been obtained by the decoupled CVEM-BEM coupling with orders $k_\Omega = 4$ for the interior CVEM and $k_\Gamma = 1$ for the BEM. The total number of degrees of freedom is 61,576.

To test the performance of the proposed method in case of non-convex artificial boundaries with re-entrant curves like the one considered, and hence the reliability of the corresponding numerical results, we compare the solution obtained in the flower-shaped domain with that retrieved in a larger one, which encloses the obstacles. To this aim, we choose the circle centered in $\mathbf{O} = (0,0)$ with minimum radius containing the flower, i.e. with radius 3.995. For both tests, we have considered $T = 10$ and $N = 512$.

As we can see, the snapshots in Figure 7 for the flower domain perfectly match with the restriction to the flower of those represented in the annulus domain. It is worth noting that, to achieve a reliable solution by a comparable mesh size $h_\Omega = 1.38\text{e}{-01}$, the choice of the larger circular domain implies higher computational cost and memory requirements. In particular, in our case, its decomposition has required 15,744 quadrilaterals. With such a choice, the total number of degrees of freedom, obtained with the same approximation orders $k_\Omega = 4$ and $k_\Gamma = 1$, is 206,780. Therefore, the feasibility in the choice of an ad hoc artificial boundary allowed us to save about 70 % in memory storage.

Conclusions and Perspectives

We have proposed a new approach for the simulation of time-domain wave fields scattered by obstacles with complex geometries in unbounded domains. For its solution, we have applied the coupling of a domain method with a boundary one, the latter associated with an integral non-reflecting boundary condition imposed on an artificial contour of arbitrary shape. The novelty of this paper consists in using a CVEM to determine the solution in the computational area limited by the artificial boundary. Among the main benefits of the CVEM, in this paper, we have exploited the easiness of constructing high-order approximation spaces associated with generic curvilinear polygons, and of using decoupled orders of accuracy for the interior and the boundary methods. The latter represents a crucial issue, the implementation of high-order boundary element methods being a difficult task, because of the necessity of computing accurately boundary integrals involving non-smooth kernels. The good performance of the proposed scheme encourages us to extend its application to other contexts such as, for example, elastodynamic exterior problems, for which accurate simulations involving a high number of degrees of freedom are required in complex geometries and over large time intervals of analysis.

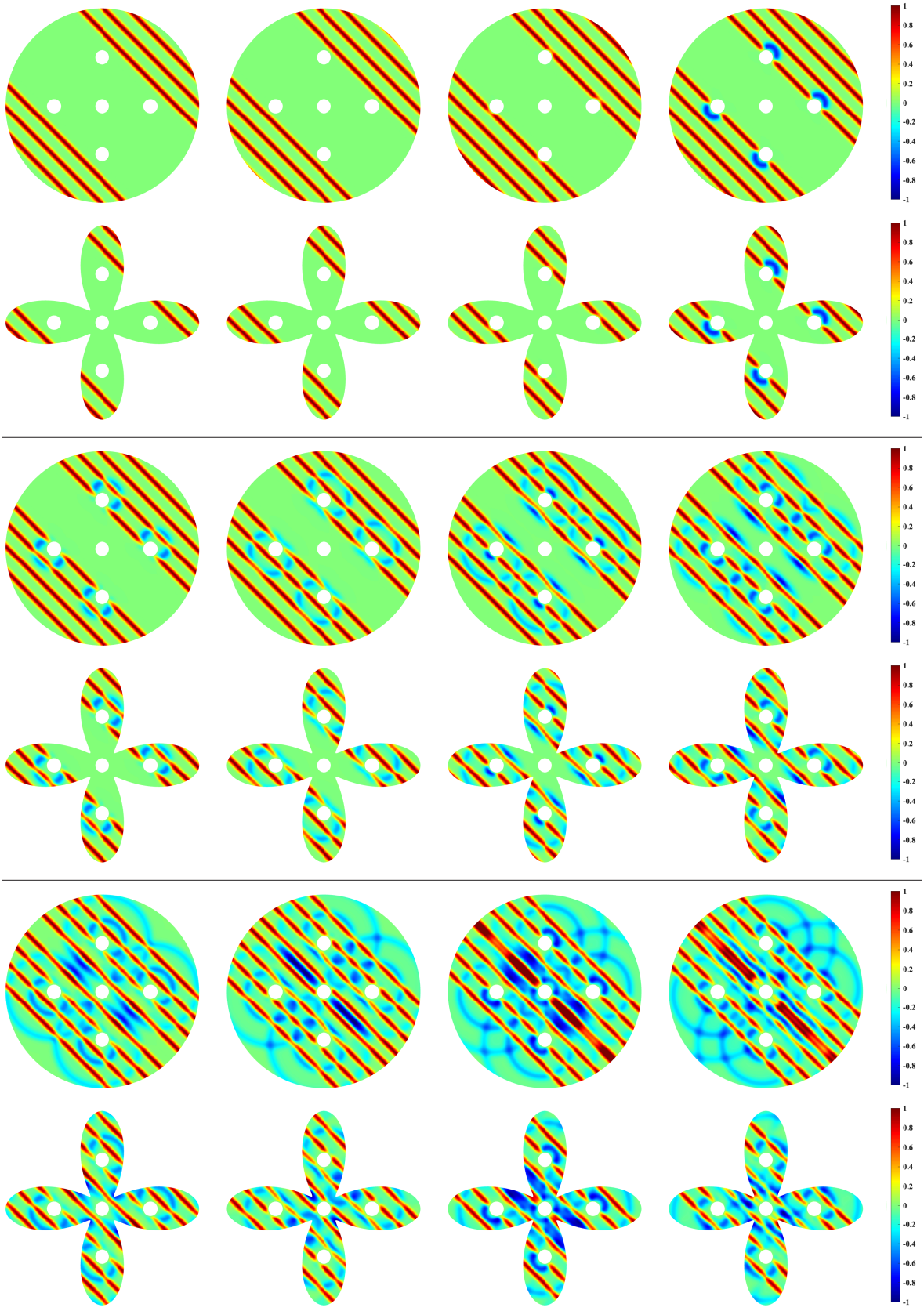

Figure 7: Example 4. Snapshots of the approximate solutions at the instants $t_{10}, t_{15}, t_{20}, t_{25}, t_{30}, t_{35}, t_{40}, t_{45}, t_{50}, t_{55}, t_{60}, t_{65}$ (from top left to bottom right).

Funding: This work was performed as part of the GNCS-INDAM 2020 research program *Metodologie innovative per problemi di propagazione di onde in domini illimitati: aspetti teorici e computazionali*. The third author was partially supported by MIUR grant *Dipartimenti di Eccellenza 2018-2022*, CUP E11G18000350001.

References

[1] B. Ahmed, A. Alsaedi, F. Brezzi, L. D. Marini and A. Russo, Equivalent projectors for virtual element methods, *Comput. Math. Appl.* **66** (2013), 376–391.

[2] A. Aimi, L. Desiderio and G. Di Credico, Partially pivoted ACA based acceleration of the energetic BEM for time-domain acoustic and elastic waves exterior problems, *Comput. Math. Appl.* **119** (2022), 351–370.

[3] A. Aimi, L. Desiderio, M. Diligenti and C. Guardasoni, A numerical study of energetic BEM-FEM applied to wave propagation in 2D multidomains, *Publ. Inst. Math. (Beograd) (N. S.)* **96(110)** (2014), 5–22.

[4] A. Aimi, L. Desiderio, P. Fedeli and A. Frangi, A fast boundary-finite element approach for estimating anchor losses in micro-electro-mechanical system resonators, *Appl. Math. Model.* **97** (2021), 741–753.

[5] P. F. Antonietti, G. Manzini and M. Verani, The conforming virtual element method for polyharmonic problems, *Comput. Math. Appl.* **79** (2020), no. 7, 2021–2034.

[6] E. Artioli, S. Marfia and E. Sacco, VEM-based tracking algorithm for cohesive/frictional 2D fracture, *Comput. Methods Appl. Mech. Engrg.* **365** (2020), Paper No. 112956.

[7] A. Bamberger and T. H. Duong, Formulation variationnelle espace-temps pour le calcul par potentiel retardé de la diffraction d'une onde acoustique. I, *Math. Methods Appl. Sci.* **8** (1986), no. 3, 405–435.

[8] L. Banjai, Multistep and multistage convolution quadrature for the wave equation: Algorithms and experiments, *SIAM J. Sci. Comput.* **32** (2010), no. 5, 2964–2994.

[9] L. Banjai, Implicit/explicit, BEM/FEM coupled scheme for acoustic waves with the wave equation in the second order formulation, *Comput. Methods Appl. Math.* **22** (2022), no. 4, 757–773.

[10] L. Banjai, C. Lubich and F.-J. Sayas, Stable numerical coupling of exterior and interior problems for the wave equation, *Numer. Math.* **129** (2015), no. 4, 611–646.

[11] L. Beirão da Veiga, F. Brezzi, A. Cangiani, G. Manzini, L. D. Marini and A. Russo, Basic principles of virtual element methods, *Math. Models Methods Appl. Sci.* **23** (2013), no. 1, 199–214.

[12] L. Beirão da Veiga, F. Brezzi, L. D. Marini and A. Russo, The hitchhiker's guide to the virtual element method, *Math. Models Methods Appl. Sci.* **24** (2014), no. 8, 1541–1573.

[13] L. Beirão da Veiga, F. Brezzi, L. D. Marini and A. Russo, Mixed virtual element methods for general second order elliptic problems on polygonal meshes, *ESAIM Math. Model. Numer. Anal.* **50** (2016), no. 3, 727–747.

[14] L. Beirão da Veiga, C. Lovadina and A. Russo, Stability analysis for the virtual element method, *Math. Models Methods Appl. Sci.* **27** (2017), no. 13, 2557–2594.

[15] L. Beirão da Veiga, A. Russo and G. Vacca, The virtual element method with curved edges, *ESAIM Math. Model. Numer. Anal.* **53** (2019), no. 2, 375–404.

[16] S. Berrone, A. Borio and F. Marcon, Comparison of standard and stabilization free virtual elements on anisotropic elliptic problems, *Appl. Math. Lett.* **129** (2022), Paper No. 107971.

[17] S. C. Brenner, Q. Guan and L.-Y. Sung, Some estimates for virtual element methods, *Comput. Methods Appl. Math.* **17** (2017), no. 4, 553–574.

[18] S. Chaillat, L. Desiderio and P. Ciarlet, Theory and implementation of $\mathcal{H}$-matrix based iterative and direct solvers for Helmholtz and elastodynamic oscillatory kernels, *J. Comput. Phys.* **351** (2017), 165–186.

[19] B. Chen, F. Ma and Y. Guo, Time domain scattering and inverse scattering problems in a locally perturbed half-plane, *Appl. Anal.* **96** (2017), no. 8, 1303–1325.

[20] M. Costabel, Symmetric methods for the coupling of finite elements and boundary elements (invited contribution), in: *Boundary Elements IX, Vol. 1* (Stuttgart 1987), Computational Mechanics, Southampton (1987), 411–420.

[21] L. Desiderio and S. Falletta, Efficient solution of two-dimensional wave propagation problems by CQ-wavelet BEM: Algorithm and applications, *SIAM J. Sci. Comput.* **42** (2020), no. 4, B894–B920.

[22] L. Desiderio, S. Falletta, M. Ferrari and L. Scuderi, CVEM-BEM coupling with decoupled orders for 2D exterior Poisson problems, *J. Sci. Comput.* **92** (2022), no. 3, Paper No. 96.

[23] L. Desiderio, S. Falletta, M. Ferrari and L. Scuderi, On the coupling of the curved virtual element method with the one-equation boundary element method for 2D exterior Helmholtz problems, *SIAM J. Numer. Anal.* **60** (2022), no. 4, 2099–2124.

[24] L. Desiderio, S. Falletta and L. Scuderi, A virtual element method coupled with a boundary integral non reflecting condition for 2D exterior Helmholtz problems, *Comput. Math. Appl.* **84** (2021), 296–313.

[25] H. Eruslu and F. J. Sayas, Polynomially bounded error estimates for trapezoidal rule convolution quadrature, *Comput. Math. Appl.* **79** (2020), no. 6, 1634–1643.

[26] S. Falletta and G. Monegato, An exact non reflecting boundary condition for 2D time-dependent wave equation problems, *Wave Motion* **51** (2014), no. 1, 168–192.
[27] S. Falletta and G. Monegato, Exact non-reflecting boundary condition for 3D time-dependent multiple scattering–multiple source problems, *Wave Motion* **58** (2015), 281–302.
[28] S. Falletta, G. Monegato and L. Scuderi, A space-time BIE method for nonhomogeneous exterior wave equation problems. The Dirichlet case, *IMA J. Numer. Anal.* **32** (2012), no. 1, 202–226.
[29] S. Falletta, G. Monegato and L. Scuderi, A space-time BIE method for wave equation problems: The (two-dimensional) Neumann case, *IMA J. Numer. Anal.* **34** (2014), no. 1, 390–434.
[30] S. Falletta and S. A. Sauter, The panel-clustering method for the wave equation in two spatial dimensions, *J. Comput. Phys.* **305** (2016), 217–243.
[31] G. N. Gatica and S. Meddahi, Coupling of virtual element and boundary element methods for the solution of acoustic scattering problems, *J. Numer. Math.* **28** (2020), no. 4, 223–245.
[32] C. Geuzaine and J.-F. Remacle, Gmsh: A 3-D finite element mesh generator with built-in pre- and post-processing facilities, *Internat. J. Numer. Methods Engrg.* **79** (2009), no. 11, 1309–1331.
[33] H. Gimperlein, C. Özdemir and E. P. Stephan, A time-dependent FEM-BEM coupling method for fluid-structure interaction in 3*d*, *Appl. Numer. Math.* **152** (2020), 49–65.
[34] H. Gimperlein, C. Özdemir and E. P. Stephan, Error estimates for FE-BE coupling of scattering of waves in the time domain, *Comput. Methods Appl. Math.* **22** (2022), no. 4, 839–859.
[35] D. Givoli, *Numerical Methods for Problems in Infinite Domains*, Stud. Appl. Math. 33, Elsevier Scientific, Amsterdam, 2013.
[36] H. D. Han, A new class of variational formulations for the coupling of finite and boundary element methods, *J. Comput. Math.* **8** (1990), no. 3, 223–232.
[37] C. Johnson and J.-C. Nédélec, On the coupling of boundary integral and finite element methods, *Math. Comp.* **35** (1980), no. 152, 1063–1079.
[38] C. Lubich, Convolution quadrature and discretized operational calculus. II, *Numer. Math.* **52** (1988), no. 4, 413–425.
[39] G. Monegato and L. Scuderi, Numerical integration of functions with boundary singularities, *J. Comput. Appl. Math.* **112** (1999), 201–214.
[40] F.-J. Sayas, The validity of Johnson–Nédélec's BEM-FEM coupling on polygonal interfaces, *SIAM J. Numer. Anal.* **47** (2009), no. 5, 3451–3463.
[41] M. Schanz, Fast multipole method for poroelastodynamics, *Eng. Anal. Bound. Elem.* **89** (2018), 50–59.
[42] A. Sommariva and M. Vianello, Product Gauss cubature over polygons based on Green's integration formula, *BIT* **47** (2007), no. 2, 441–453.
[43] A. Sommariva and M. Vianello, Gauss–Green cubature and moment computation over arbitrary geometries, *J. Comput. Appl. Math.* **231** (2009), no. 2, 886–896.
[44] O. Steinbach, A note on the stable one-equation coupling of finite and boundary elements, *SIAM J. Numer. Anal.* **49** (2011), no. 4, 1521–1531.
[45] F. Xie, Y. Qu, M. A. Islam and G. Meng, A sharp-interface Cartesian grid method for time-domain acoustic scattering from complex geometries, *Comput. & Fluids* **202** (2020), Paper No. 104498.